

Theoretical Study of the Stability of Au_nGe_m Clusters

Danielle McDermott^{1a} and Kathie E. Newman^{2b}

¹ Department of Physics, Wabash College, Crawfordsville, IN 47933

² Department of Physics, University of Notre Dame, Notre Dame IN 46556

Received: date / Revised version: date

Abstract. We investigate the properties of clusters formed from two connected Ge_m cage-like clusters, such as experimentally synthesized $Au_3Ge_{18}^{5-}$, using first-principles DFT methods. We focus particularly on $Au_nGe_{12}^{q-}$ formed from Ge_6 , where $n = 0 - 3$ and $q = 0, 2$. We examine the geometries, electronic structure, and thermal excitations of these clusters using the SIESTA code, where we test stability using short molecular dynamics simulations. Our examination of intercluster bridges between Ge_m , formed of either Ge-Ge or Au-Ge bonds, indicates that the overlap of interacting molecular orbitals of Ge_m can either bind a cluster together or tear it apart depending on the orientation of the bridging atoms with respect to the cages. We characterize the properties of stable isomers of neutrally charged $AuGe_{12}$ and Au_2Ge_{12} , seeing that radially directed molecular orbitals stabilize $AuGe_{12}$ while a geometric asymmetry stabilizes Au_2Ge_{12} and Au_3Ge_{18} . We examine a two-dimensional ${}_{\infty}^2[Au_2Ge_6]$ structure, finding it more stable than other periodic $[Au_nGe_6]$ subunits. We observe no stable neutral isomers of Au_3Ge_{12} , but see that additional charge supports isomers of both Au_2Ge_{12} and Au_3Ge_{12} .

PACS. 31.15.A 36.40.c 61.46.Bc

1 Introduction

Gold-Germanium alloys are important and interesting both from the perspective of basic science and technological application. The binary, eutectic Au-Ge system [1] displays bulk diffusion, phase separation, and subsequent crystallization of well separated Au and Ge [2,3]. Large spacing ions can stabilize crystalline solids such as $ScAuGe$ and $SrAu_3Ge$ which contain hexagonal planes of Au-Ge structure [4] and octahedra of Au_5Ge [5], respectively. Studies of Au atoms on Ge surfaces reveal a Luttinger-liquid like state [6] and Au is often used in catalyzing reactions in Ge. In nanoscale applications, the eutectic and catalytic behavior is less predictable, yet phase separation still drives interesting pattern formation such as Au-catalyzed Ge-nanowires [8,9,10,11]. Experimentalists and theorists alike have made significant progress in understanding the overall nanowire growth process, through the use of in-situ video rate TEM [12] and semi-empirical models [13,14]. Yet an atomic-scale description of Au-Ge bonds is essential for a broader physical understanding of these kinetic processes.

Compelling clusters of Au-Ge include $AuGe_{18}$ [15], $Au_3Ge_{18}^{5-}$ [16], and $Au_3Ge_{45}^{9-}$ [17] which are formed from linked Ge_9^{q-} clusters and stabilized with counterions. The building blocks Ge_9^{q-} are found experimentally as $[Ge_9]^{4-}$

Zintl ion clusters and within many Zintl solids including Cs_4Ge_9 [18]. Such Ge Zintl ions are stabilized by delocalized electrons, follow Wade's Rules [19,20], and reveal bonding environments beyond the sp^3 bonds of bulk Ge structures [21]. Importantly, these Ge_9^{q-} clusters provide a method of synthesizing crystalline and micro-crystalline Ge solids [22,23,24] such as the synthesis of expanded phase Ge_{136} by the oxidation of the Ge_9^{4-} Zintl anion by an ionic liquid [25].

While Ge_9^{q-} Zintl cages are widely studied, six-atom Ge clusters could provide an alternate pathway to growing Ge based materials. In this paper, we ask the following: Can Au link together other small Ge clusters? What does this teach us about Au-Ge bond lengths and angles? How does this depend on the electronic properties of the Ge cluster? Using density functional theory, our work examines cluster ions Ge_6^{q-} and $Au_3Ge_{18}^{q-}$, which have been previously studied in experiment, and a theoretical series of $Au_nGe_{12}^{q-}$ clusters, where $n = 0 - 3$, that have a range of stability and electronic behavior which may indicate how stable Au-Ge bonds form.

We use the octahedral shaped Ge_6^{2-} as a model cluster, in part because its O_h symmetry yields a significantly reduced set of possible Au-Ge bond angles to explore. Furthermore the O_h symmetry follows Wade's rules, which connect the overall shape of a cluster with n vertices to its number of skeletal electron pairs, therefore a deformation away from octahedrality indicates whether excess charges have localized in the intercluster bridging struc-

^a email: mcdermod@wabash.edu

^b email: newman@nd.edu

ture or the Ge cage region of $\text{Au}_n\text{Ge}_{12}^{q-}$ clusters. Such Ge_6 cages have been experimentally synthesized in gas phase [26] and solids [27,28]. Richards *et al.* isolated the octahedral Ge_6 cluster, stabilized by organic groups, with reductive coupling [29]. Ge_6 cages have been studied computationally [30,31] with a focus on the effects of ionic charge on cluster geometry: neutral Ge_6 flattens to a C_{2v} symmetry while ionic Ge_6^{2-} has octahedral O_h symmetry. The neutral Ge_6 geometry was also observed by Zhao *et al.* in a computational study which focused primarily on fragmentation behavior in Ge_n clusters, and indicates Ge_6 as a common fragment of larger clusters [32].

Au-Ge bonds lack a simple descriptive model that can simultaneously treat both the electron delocalization typical of metals and the localized bonds typical of semiconductors. Thus their treatment requires a first principles, or *ab initio*, approach, that uses flexible basis sets to capture a variety of bond hybridizations. While *ab initio* calculations are computationally expensive, alternative models that parameterize metal-semiconductor bonding with empirical potentials have not provided accurate descriptions of bond-angles in small clusters [13,14]. Thus we use first principles density functional theory (DFT) implemented with the SIESTA (Spanish Initiative for Electronic Simulations with Thousands of Atoms) code [33,34].

Previous Ge and Au-Ge cluster studies have focused on the configurational entropy of N atoms [36,37,38,39], which is the essential concern of many DFT cluster studies. Such studies [40,41] confirm that small gas phase Au-Ge clusters are amorphous, as observed experimentally [42]. Recent studies have focused on endohedral Ge clusters encapsulating a metal ion [43,44]. These previous studies examine electronic structure, vibrational frequencies, and cluster fragmentation properties, but molecular dynamics (MD) simulations at the DFT level are rare due to their computational expense.

In Sec. 2 we describe our computational methods in modeling neutral and charged clusters. Our general technique initializes the atomic positions in SIESTA with a hand-picked geometry and applies the Conjugate Gradient algorithm (CG) to relax the positions to a local minima. We focus on clusters similar to $\text{Au}_3\text{Ge}_{18}^{5-}$ which feature two well-separated Ge clusters connected with $n = 0 - 3$ Au atoms. This requires an alternative to advanced sampling techniques such as metadynamics [45] or a Genetic Algorithm [39], which tend to calculate compact structures in their search for global energy minima. We consider the gas-phase (isolated) clusters with DFT, MD, and electronic structure studies, but acknowledge the necessity of counterions in experiment. As we predict new possible Au-Ge structures, these theoretical geometries may appear metastable, yet contain Au-Ge bonds that could be observed with ligand stabilization. We search for stabilizing trends in symmetric Au-Ge clusters, examining both internal bonds, which define an individual Ge_6 cage geometry, and external bonds, which describe how Ge_6 cages link to each other or with a bridge of Au atoms.

Our results, presented in Sec. 3, describe ground state cluster properties (geometry and electronic structure) and

examine cluster stability with molecular dynamics at temperatures near the bulk eutectic temperature $T_E = 361^\circ\text{C}$, where presumably small, unstable molecules will “melt” completely. The geometry analysis uses Wade’s Rules, examining the deviation of the cluster from perfect symmetry and its overall electron count, and reports typical bondlengths and angles. Our analysis of electronic states includes Molecular Orbitals (MO), Density of States (DOS), and an electronic partitioning method, Crystal Overlap Hamiltonian Population (COHP) [46].

In Sec. 3.1 we describe the electronic structure of Ge_m^{q-} , where $m = 6, 9, 12$, while comparing their geometries to both previous calculations and experimental measurements. We compare these to hypothetical Ge_{12} clusters composed of two Ge_6 cages in Sec. 3.2. After characterizing pure Ge clusters, in Sec. 3.3 we introduce Au-Ge clusters by describing calculated properties of the experimentally observed $\text{Au}_3\text{Ge}_{18}^{q-}$. In Sec. 3.4 we investigate ground-state properties of clusters with stoichiometry $\text{Au}_n\text{Ge}_{12}$ composed of different configurations of two Ge_6 cages with $n = 1 - 3$. In Sec. 3.5, we explore the stability of these configurations under molecular-dynamics simulations. We describe the effects of electronic charge on cluster properties in Sec. 3.6. Next we compare the electronic structures and stabilities of all clusters using the COHP in Sec. 3.7 to examine what constitutes a chemical bond. Finally in Sec. 3.8, we propose a new extended two-dimensional (2D) structure built upon Ge_6 cages. Our work uniquely examines the the COHP properties of certain experimentally observed clusters, and extends the observations to examine the properties defining stability in Au-linked Ge clusters. We discuss our conclusions on electronic and geometric properties which lend overall stability to such clusters in Sec. 4.

2 Methods

We have carried out electronic structure calculations with the fully *ab initio* DFT code SIESTA [33,34] which uses Troullier-Martins norm-conserving pseudopotentials [47] in the Kleinman-Bylander form [48]. The Kohn-Sham [49] wave function was expanded with basis sets of the localized atomic orbitals (LCAO) of the method by Sankey and Niklewski [50]. The localization is a key advantage in studying charged states in molecular or nanosized systems. We use Double-Zeta Polarized (DZP) orbitals and the Generalized Gradient Approximation (GGA) of Perdew, Burke, and Ernzerhof [51] for the exchange-correlation energy functional.

Our Ge basis set has cutoff radii for the $4s$ orbital of 7.12, 1.92 Bohr; $4p$ of 7.72, 4.92 Bohr; and a polarization orbital $4d$ with a cutoff of 7.79 Bohr [52]. The Au basis set has cutoff radii of $5d$: 7.20, 5.57 Bohr; $6s$: 6.50, 5.50 Bohr; and a polarization orbital $6p$: 5.85 Bohr. We use soft-confinement potentials and an ionic core to create basis orbitals [53]. The Au pseudopotential includes the semicore $5d^{10}$ states [54,55,56]. Both Au and Ge use a partial-core correction to treat overlap between valence and core electrons.

The charge density was represented on a real-space grid with an energy cutoff of 100 Ry. A Monkhorst-Pack k -point mesh of $10 \times 10 \times 10$ ensured convergence. We used a Conjugate Gradient (CG) minimization with a maximum force tolerance of $0.04 \text{ eV}/\text{\AA}$ to reveal the local coordinate relaxations. For our molecular dynamics (MD) runs, we use the Nosé thermostat [57] to simulate the canonical ensemble (NVT) with a Nosé mass of 200 Ry fs^2 . We test the stability of our systems by subjecting them to a temperature of 600K during 1000 steps, each of 2 fs, as suggested by Ref. [55].

The COHP uses DFT matrix elements to separate electronic bonding states from antibonding states in the DOS. In both the DOS and COHP curves we use a small smearing value, $s \approx 0.1$, and a high number of sampling points, $n \approx 500$, to create smooth electronic structure curves. We treat neighbor interactions within 0.4\AA of the maximal considered ‘‘bond’’ lengths [58]. In examining the electronic states, we focus on the hybridization of the levels presented as indicators of electron delocalization.

3 Results

3.1 Calibration of SIESTA with Ge Clusters

Ge is an example of a main-group element that participates in delocalized cage bonding. It can be analyzed in terms of Wade’s rules [19,20], which connect the shape of a cluster with n vertices to its number of skeletal electron pairs. The clusters Ge_6 and $[\text{Ge}_6]^{2-}$ have analogous shapes to BH_6 and $[\text{BH}_6]^{2-}$ clusters; where $[\text{Ge}_6]^{2-}$ will form an octahedron (or *closo* 6-vertex polyhedron). Similarly Ge_9^{4-} forms a *closo* 9-vertex polyhedron, while Ge_{12} does not follow Wade’s Rules [59].

Using CG minimization in SIESTA, we initialize the geometries of Ge_6 and $[\text{Ge}_6]^{2-}$ clusters as octahedra with atomic coordinates $\pm(a, 0, 0)$, $\pm(0, a, 0)$, $\pm(0, 0, a)$ using $a \approx 2.12 \text{\AA}$, or initial Ge-Ge separations of 3.0\AA . In the relaxed clusters we find the same geometries as King *et al.* [31] where Ge_6 flattens to C_{2v} symmetry and ionic $[\text{Ge}_6]^{2-}$ has the expected octahedral O_h symmetry. Calculating a minimum and maximum relaxed Ge-Ge distance in Ge_6 , we find respectively 2.53\AA and 2.85\AA , compared with previous calculations of 2.58\AA and 2.81\AA [31] and 2.47\AA and 2.85\AA [30]. Our calculated bond length, 2.68\AA , for octahedral $[\text{Ge}_6]^{2-}$ compares favorably with that of 2.69\AA from Ref. [31], and has been measured to be 2.63\AA [29] in a ligand stabilized system.

We characterize cluster symmetry using the deviation, σ_{d_G} , of the cluster from a perfect octahedron by averaging over the twelve skeletal Ge-Ge distances of a single cluster: $\bar{d}_G \pm \sigma_{d_G}$. A perfect octahedral cluster is composed of twelve identical bonds with $\sigma_{d_G} = 0.0 \text{\AA}$. Some deformation from O_h symmetry may occur while σ_{d_G} remains zero; for instance we observe Ge_6^{2-} has nearly identical bondlengths such that $\sigma_{d_G} = 0.0 \text{\AA}$ yet it is slightly flattened. The neutral Ge_6 cluster with C_{2v} symmetry yields $\bar{d}_G = 2.68 \pm 0.20 \text{\AA}$. In calculating σ_{d_G} for our larger

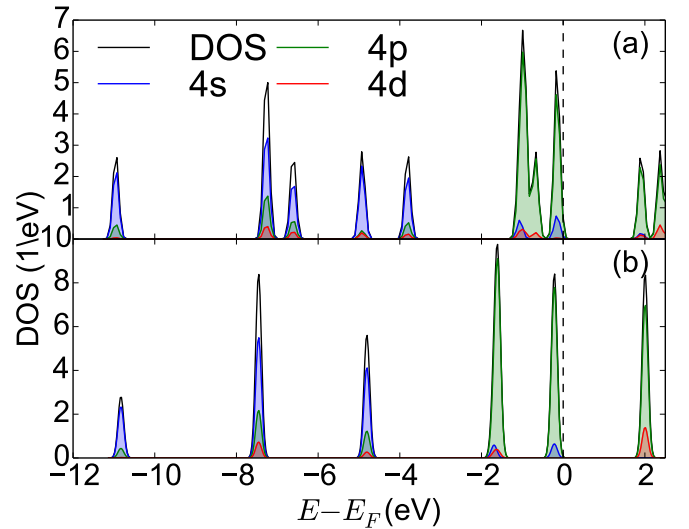


Fig. 1. Calculated densities of states (DOS) versus energy (eV) for (a) Ge_6 and (b) $[\text{Ge}_6]^{2-}$ where the total DOS is black, the $4s$ orbital is blue, $4p$ is green, and $4d$ is red. Contributions from other orbitals have not been treated.

$\text{Au}_n\text{Ge}_{12}$ clusters, we treat each Ge_6 separately and we do not include intercluster bonds. Moreover, for deformed Ge_6 cages, the skeletal Ge-Ge distances can elongate well beyond typical Ge-Ge bond lengths. Thus we have adapted σ_{d_G} to be a measure of the deviation from octahedrality of a given Ge_6 cage.

We show our calculated total (DOS) and partial (pDOS) density of states of (a) Ge_6 and (b) Ge_6^{2-} in Fig. 1. The pDOS shows orbitals dominated by $4s$ character below $E - E_F = -2.0 \text{ eV}$ and by $4p$ in the range $-2.0 \text{ eV} < E - E_F < 0.0 \text{ eV}$. We observe this characteristic orbital behavior in both pure Ge clusters and Au-Ge clusters throughout this study. In the neutral Ge_6 cluster, we see a stronger hybridization of atomic states, as shown in Fig. 1(a) when compared with (b) $[\text{Ge}_6]^{2-}$, which is further confirmed in examining the MOs.

In Figure 2 we show the MOs and corresponding energy levels (within $\pm 0.1 \text{ eV}$) of (a) Ge_6 and (b) $[\text{Ge}_6]^{2-}$. We find that our calculated MO energy levels for Ge_6 and $[\text{Ge}_6]^{2-}$ compare favorably to the results found by King *et al.* [31]. The overall symmetries and degeneracies match Table 5 in Ref. [31], however we observe an overall difference in the magnitude of the energy levels. Due to different basis sets, we calculate a consistent energy shift approximately 2-3 eV for $[\text{Ge}_6]^{2-}$ and 5.5-6.5 eV for Ge_6 . The energy levels of Ge_6 and $[\text{Ge}_6]^{2-}$ differ in part due to degeneracies available in the O_h symmetry for $[\text{Ge}_6]^{2-}$ which are not available in the C_{2v} symmetry of Ge_6 . We observe MOs to be more localized on atomic centers in Ge_6 than in $[\text{Ge}_6]^{2-}$. We see the two additional electrons in $[\text{Ge}_6]^{2-}$ shift the Fermi energy, E_F , upward and allow a thirteenth orbital to be occupied. This presumably drives the symmetry change to O_h , with p electrons now able to reside in a cubic environment.

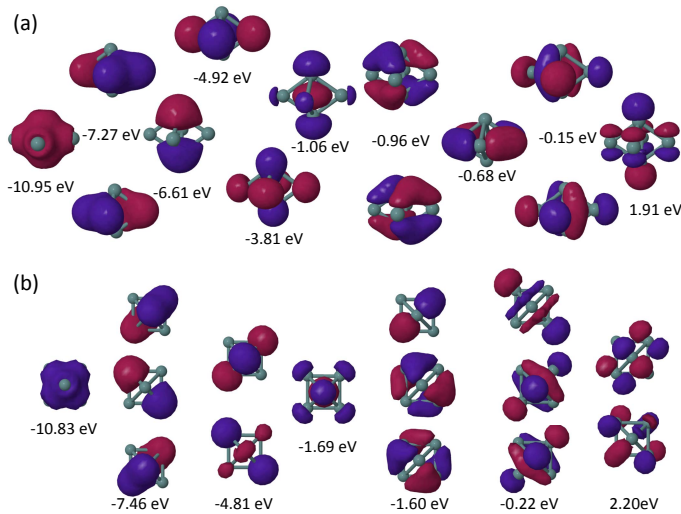


Fig. 2. Molecular orbitals of (a) Ge_6 and (b) Ge_6^{2-} .

We briefly describe Ge_9 and Ge_{12} to complete our calibration of the SIESTA code. We initialize the CG relaxation using previously reported geometries. Much like our detailed description of Ge_6 , we observe very similar clusters to those previously calculated in Refs. [32, 59, 60, 61] both in geometry and electronic structure. Consistent with Wade’s rules, we observe the symmetry of Ge_9^{q-} increases to D_{3v} with $q = 2$ and C_{4h} with $q = 4$ as in Ref. [61]. As in Ref. [59], the low energy isomer of the Ge_{12} cluster deviates from Wade’s Rules and resembles a tetracapped cube with C_{2v} symmetry [Fig. 3(a)]. We see a qualitative agreement in the MOs, with the same symmetries and approximate energies levels as previously reported.

We conclude by calculating binding energies, E_B , and Fermi gaps, E_{gap} (Table 1) of Ge_m clusters. E_B is calculated as:

$$E_B = \frac{E_T - (N_A E_A + N_G E_G)}{N_A + N_G} \quad (1)$$

where N_A and N_G are the total number of Au and Ge atoms, and E_T , E_A , and E_G are the SIESTA calculated total energies for the cluster and isolated atoms, respectively. Our calculation shows systematically higher E_B , than previously reported for pure Ge clusters. The systematic difference in E_B is consistent with cohesive energies calculated with SIESTA in Ref. [34] for bulk Si and elsewhere. While our values of E_{gap} differ, given slight deformations in the geometries, and the known underestimates of E_{gap} within GGA calculations, we consider our values reasonable comparisons to previous calculations.

3.2 Ge_{12} Clusters: Relaxed Geometries and DOS

Next we examine isomers of Ge_{12} formed by joining two Ge_6 together with one or two intercluster bonds. While these will not result in groundstate Ge_{12} clusters, they provide a comparison to $\text{Au}_n\text{Ge}_{12}$ clusters examined in Sec. 3.4. We initialize each Ge_6 cluster as an octahedra, again with initial Ge-Ge separation of 3.0\AA , and change

Table 1. Calculated E_B and E_{gap} (eV) of CG-relaxed clusters Ge_6 , Ge_9 , and Ge_{12} (Z_0) from this work and those of Ref. [32] in parentheses.

	Ge_6		Ge_9		Ge_{12} Z_0	
E_B	4.425	(3.092)	4.589	(3.215)	4.650	(3.270)
E_{gap}	2.05	(1.992)	1.24	(1.676)	1.59	(2.003)

Table 2. Average skeletal distance \bar{d}_G , deviation from octahedrality σ_{d_G} , range of bond lengths d_G , intercluster distances d_i (all distances in \AA), and binding energy per atom E_B (eV) calculated for the CG-relaxed clusters Ge_{12} .

Ge_{12}	\bar{d}_G	σ_{d_G}	d_G	d_i	E_B
Z_0	—	—	1.90-2.80	—	4.650
I_0	2.667	0.104	2.55-2.80	2.56	4.527
II_0	2.683	0.182	2.55-2.93	2.68	4.475
III_0	2.667	0.064	2.57-2.77	2.64-2.80	4.474

their relative orientation. Here we present the initial configurations of three such Ge_6 - Ge_6 clusters and their CG-relaxed geometries. We describe three configurations in terms of two local Cartesian coordinate systems (x, y, z) and (x', y', z') for each cluster. We present our clusters in order of highest to lowest binding energy (following CG relaxation), starting from I_n , where n denotes the number of Au atoms. We will compare these clusters with the C_{2v} symmetry Ge_{12} cluster described in Sec. 3.1. We label the ground state as Z_0 since it is outside our schema of coupled Ge_6 clusters.

In configuration I_0 , the axes (x, y, z) and (x', y', z') differ by a linear translation so that all axes point respectively in the same directions and the atoms in the two equatorial planes xy and $x'y'$ form two intercluster Ge-Ge links pointing locally along directions $\hat{x} + \hat{y}$ and $-\hat{x}' - \hat{y}'$. In configuration II_0 , the two sets of axes again point in the same directions and a single intercluster link forms in the local directions \hat{x} and $-\hat{x}'$. In configuration III_0 , the two octahedra are aligned so that two triangular faces of opposing octahedra are in parallel planes and three intercluster links form a prism.

We summarize our results for the CG-relaxed clusters Ge_{12} in Table 2 and Fig. 3. The values of E_B of all isomers are close to that of the ground state. II_0 and III_0 are nearly degenerate despite their different geometries. In Fig. 3 we show the CG-relaxed and MD “temperature shaken” geometries of each isomer, reserving description of the post-MD structures until Sec. 3.5, and proceed to describe the CG-relaxed configurations. The Z_0 tetracapped cube has a relatively compact structure including a short Ge-Ge bond of 1.90\AA , and no octahedral structure (and thus we cannot measure $\bar{d}_G \pm \sigma_{d_G}$ or d_i in Table 2). The I_n clusters remain similar to their input geometries by maintaining nearly octahedral Ge_6 cages and similar intercon-

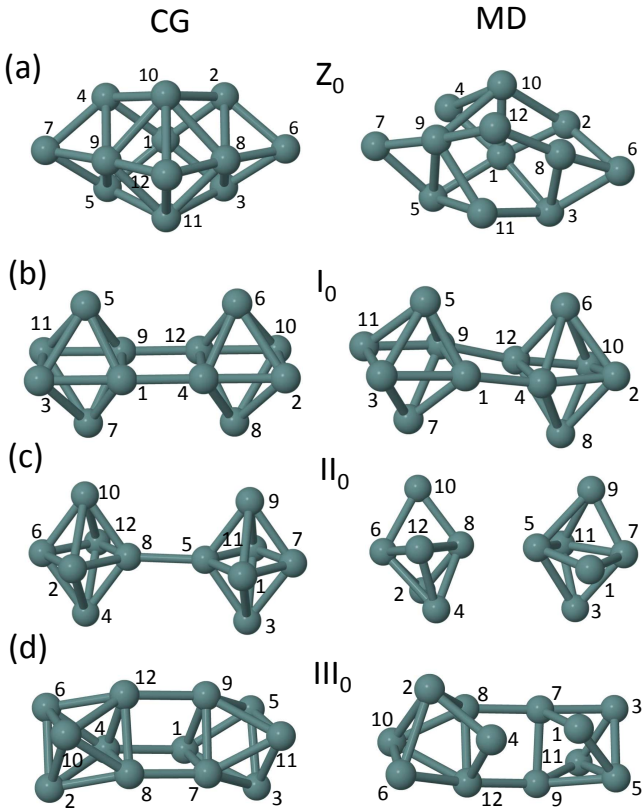


Fig. 3. Ge_{12} clusters (a) Z_0 ; (b) I_0 ; (c) II_0 ; and (d) III_0 . The left column shows relaxed geometries from CG minimization and the right shows the clusters after a MD run. The structures are all rotated slightly to show the geometry of the interconnections[58]. Ge atoms are gray.

nections. II_0 has the most deformation with $\sigma = 0.182\text{\AA}$. I_0 maintains two intercluster bonds d_i of 2.56\AA and II_0 has one of length 2.68\AA , while III_0 deforms so that it has one strong intercluster bond of $d_i = 2.64\text{\AA}$ and two elongated connections of $d_i = 2.80\text{\AA}$ which are much longer than a typical bulk Ge-Ge bond, but not unusual within a nanocluster or cage geometry. Given that DFT cannot easily identify bonds, there is some question regarding the strength of these two elongated bonds in III_0 . Since its energy is nearly that of II_0 , these bonds appear weak, which is confirmed during MD simulation.

In Fig. 4 we present the DOS of the CG-relaxed Ge_{12} structures. In (a) the DOS of Z_0 shows the $4s$ orbitals at $-6.0 < E - E_F < -4.0$ eV remain well separated with a similar magnitude as neutral Ge_6 . The $4p$ states range over $-4.0 < E - E_F < 0.0$ eV, again of similar magnitude to Ge_6 , but with a much broader range, indicating the many possible orientations of p orbitals in a tetracapped cube compared with an octahedron. The placement of the Fermi level at the center of the energy gap indicates this is a stable, insulating cluster. In (b) the DOS of I_0 we see a similar set of $4s$ and $4p$ states below E_F , with additional states at E_F itself. These are likely due to the overlap of

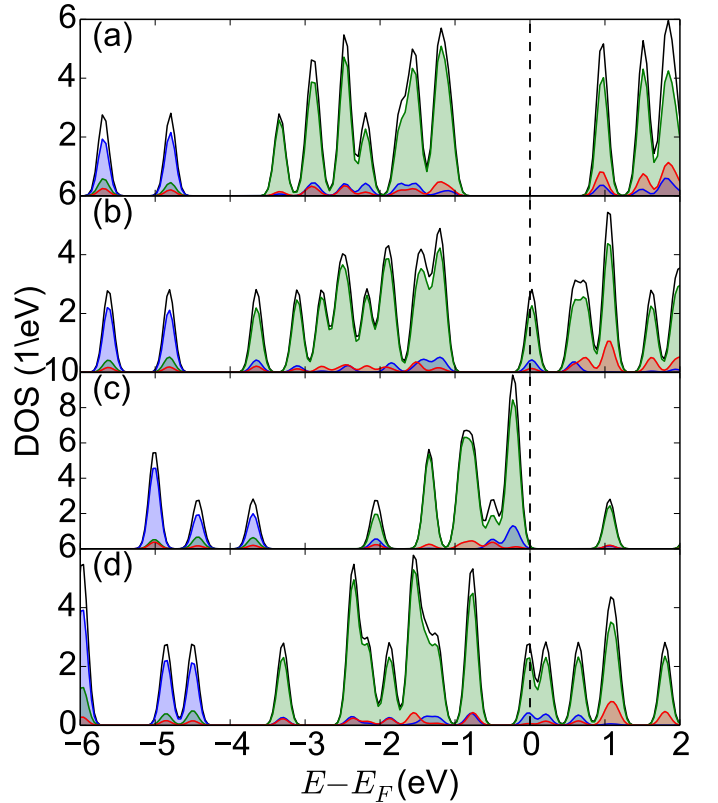


Fig. 4. DOS of CG-relaxed Ge_{12} isomers: (a) Z_0 , (b) I_0 , (c) II_0 , (d) III_0 (see Fig. 1 for color key).

the two intercluster Ge-Ge bonds. The placement of E_F indicates these states are metallic. Conversely in (c) the DOS of II_0 is similar to that of Ge_6 in Fig. 1(a). While the two highest $4s$ orbitals remain of similar magnitude to those of the other Ge_{12} clusters, like Ge_6 they are located at $-4.5 < E - E_F < -3.0$ eV. There is greater symmetry indicated in this cluster, with the $4p$ orbitals in the range $-2.5 < E - E_F < 0.0$ eV, and higher/fewer peaks than the other Ge_{12} clusters, again much like an individual Ge_6 cluster. The II_0 cluster is insulating since E_F is at the base of E_{gap} like neutral Ge_6 . The MD simulation will confirm that II_0 is readily broken into two separated Ge_6 clusters, so it is unsurprising that the overall DOS is qualitatively similar to neutral Ge_6 . The additional peaks result from more available electronic states in Ge_{12} than Ge_6 , but we observe no states that may be clearly tied to the single intercluster bond. In (d) we show that III_0 is metallic with many states in E_{gap} . The DOS is similar to that of I_0 , yet the $4s$ states at $-5.0 < E - E_F < -4.2$ eV are closer together, there are fewer peaks in the $4p$ orbitals, $-4.5 < E - E_F < -0.9$ eV, and there is a double peak at E_F . Again, the state is metallic, indicated the delocalized nature of the Ge-Ge connections in the intercluster bridging structure.

From the E_B and DOS calculations, we confirm the Ge_{12} Z_0 isomer is stable and conclude structures I_0 and III_0 have developed strong intercluster bonds while II_0 has not. While Z_0 has a large E_{gap} , I_0 and III_0 do not, and furthermore their E_F values are placed at the top of a

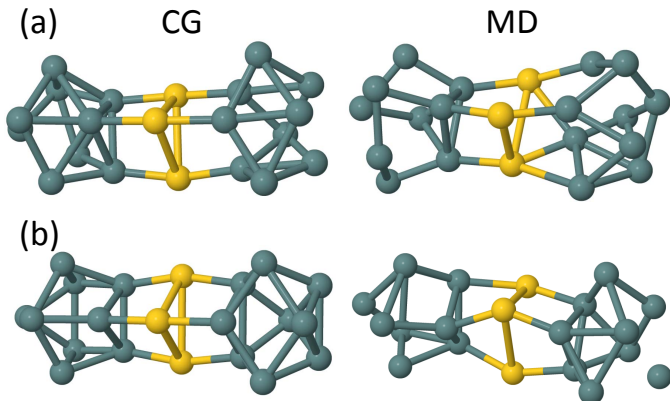


Fig. 5. $\text{Au}_3\text{Ge}_{18}^{q-}$ clusters with charge (a) $q = 0$ and (b) $q = 5$ Au atoms are gold and Ge atoms are gray.

seemly large gap, probably due to their intercluster bridging structures. Conversely II_0 seems not to have formed a strong bridging structure, instead appearing as two closely spaced Ge_6 clusters. Our examination of E_B and DOS for these Ge_{12} clusters does not clearly identify whether these new isomers are stable, but do give some perspective on whether the isomer is composed of two interacting Ge_6 clusters or a more stable, bridged Ge_{12} cluster. In latter sections, we will use MD and COHP analysis to evaluate stability in these isomers.

3.3 $\text{Au}_3\text{Ge}_{18}$ Clusters

Next we study CG-relaxed structures for $[\text{Au}_3\text{Ge}_{18}]^{5-}$ and its neutrally charged counterpart in vacuum to compare with the experimentally observed structure. As shown in Fig. 5, this structure consists of two deltahedron-shaped Ge_9 cages linked by three Au atoms. The three Au atoms bond to three Ge atoms in each cage, forming a prism-like interconnection. Since this figure highlights the interconnection, we mention the asymmetry of the clusters: the apex of one Ge_9 cage points along an apex of the prism while the opposing cage's apex points in the opposite direction (see Ref. [17]). In comparing the neutral and charged CG-relaxed structures, we observe a very similar intercluster bridge, but the neutrally charged cluster has relatively elongated Ge-Ge bonds [Fig. 5(a)], so that a complete Ge_9 deltahedron does not form. In Table 3, we summarize our results, comparing them with Spiekermann *et al.* [17], who reported bond lengths from experimental measurements and DFT calculations using a hybrid exchange and correlation (XC) functional. Experimental values for the Au-Au bond lengths, 2.900 to 3.095 Å, are shorter than calculated values. As in experiment, we observe that Ge-Ge bonds adjacent to Ge-Au bonds are considerably shorter than other Ge-Ge bonds. We also compare the three angles $\theta = \theta_{\text{Ge-Au-Ge}}$ of the intercluster linking prism in the Table 3, finding them to be in reasonable agreement with experiment. We conclude that without the presence of stabilizing ligands SIESTA has successfully reproduced the structures found experimentally.

Table 3. Ranges of calculated bond lengths (Å) found for Ge, Au-Ge, and Au-Au bonds for $[\text{Au}_3\text{Ge}_{18}]^{q-}$. Also shown, values for the angles θ connecting Au to the two cages.

q	d_G	d_{AG}	d_A	θ	Ref.
0	2.5-2.85	2.46-2.48	3.11-3.19	165°-174°	
5-	2.56-2.86	2.53	3.03-3.34	165°-172°	
5-	2.55-2.88	2.45-2.46	2.900-3.095	168°-174°	[16]

We calculated the binding energy E_B for the neutral cluster as 4.427 eV, which compares well other calculations in this work. Our calculated E_{gap} is considerably smaller than reported by Ref. [17]. Given the superiority of hybrid XC functionals for estimating optical gaps, this is unsurprising. However since our calculations show a stable cluster with a well-separated energy gap with the Fermi level at its base, which indicates overall cluster stability.

In Fig. 6 we present (a) the total DOS and species pDOS, (b) the Ge pDOS of orbitals 4s, 4p, and 4d, and (c) the Au pDOS of orbitals 5d, 6s, and 6p of the neutral cluster. The strongest Au-Ge mixing appears just below E_F where the Au 5d states mix with the Ge 4p states. Below $E - E_F < -5.0$ eV the states are dominated by Ge 4s and between $-5.0 < E - E_F < -2.0$ eV they are dominated by Au 5d states. Here E_F falls just below a larger gap, indicating a weakly conducting or insulating cluster. In (b) we observe similar Ge orbitals to those in the pure Ge_{12} clusters with well separated 4s and 4p states. One sees these 4p orbitals have considerable hybridization and peak at $E - E_F \approx 1.5$ eV, much like the neutral Ge_6 cluster. In (c) one sees the 5d orbitals of Au in the region from $-4.5 < E - E_F < 0.5$ eV, which only strongly mix with the 6s orbital in the range $-1.5 < E - E_F < 0.5$ eV. The Fermi level is just below E_{gap} , indicating a weakly metallic nature in this cluster, and the highest occupied MO is of mainly 4p character, as shown in Fig. S1.

The electronic structure of $\text{Au}_3\text{Ge}_{18}^{5-}$ is quite similar to the neutral cluster, however E_F sits at the top of E_{gap} , which indicates it is unstable without external ligands. Indeed, we observe considerable rearrangement of both neutral and charged clusters under MD simulation, as shown in Sec. 3.5, which restores the electronic structure to a stable configuration.

3.4 $\text{Au}_n\text{Ge}_{12}$ Clusters: Geometry and DOS

Now we examine linked $\text{Ge}_6\text{Au}_n\text{Ge}_6$ configurations to compare with $\text{Au}_3\text{Ge}_{18}$. There are innumerable combinations of two octahedral Ge_6 cages connected to one or more Au atoms, so we focus on input geometries that were designed to test the linearity of Ge-Au-Ge links and accommodate the symmetries of the Ge_6 cages. We tried many such input geometries, but illustrate just a few of the most interesting cases which have similar initial Ge_6 orientations as

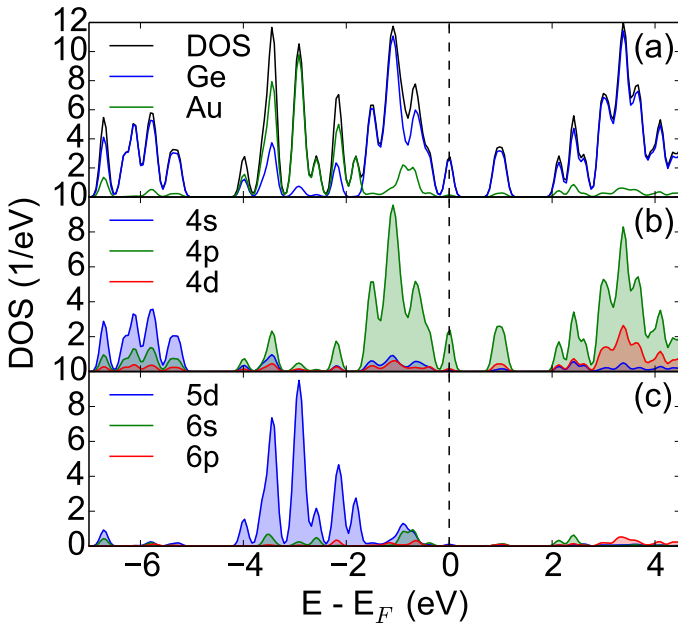


Fig. 6. The electronic structure of $\text{Au}_3\text{Ge}_{18}$ (neutrally charged) (a) DOS (black), Ge pDOS (blue) and Au pDOS (green), (b) Ge 4s (blue), 4p (green), and 4d (red), and (c) Au 5d (blue), 6s (green), and 6p (red).

those described in Section 3.2, now with intercluster Au atoms.

With just one Au atom, we examined orientations very similar to the CG structures I_0 and II_0 with an Au atom added. For both of these orientations, the axes of the octahedra are aligned with an Au atom at their midpoint. The input structure for I_0 produced I_1 , where a total of four Au-Ge links could form in the equatorial planes of the two octahedra. Likewise II_0 and II_1 shared input structures where the added Au atom in II_1 created two Au-Ge links in a line connecting the apexes of the two octahedra. With two Au atoms, many possible interlinked combinations exist, but stable isomers resulted from placing both Au atoms in the common equatorial plane of the two octahedra, creating four Au-Ge links. With three Au atoms, we focused on canted octahedra, similar to structure III_0 [Fig. 3(c)], to create a nine-atom prism much like that in $\text{Au}_3\text{Ge}_{18}$.

Such initialization procedures requires an exploration of geometry phase space to ensure our CG relaxations do not find highly metastable states. To ensure a more complete sampling of the possible configurations we use a “geometry sweep” much like the approach used to find the groundstate of crystal structures in DFT methods. In general, a sweep was generated by using as a variable the *initial* separation d_{init} of Au from Ge atoms to which it was interconnected. For a given initial cluster orientation, independent CG relaxations of the cluster were run for a series of Au-Ge separations, yielding many isomers to compare, each with a relaxed geometry and binding energy. A single geometry sweep explored one input orientation with 15-20 different Au-Ge separations while setting initial Ge-Ge distances at 3.0\AA . The CG relaxations re-

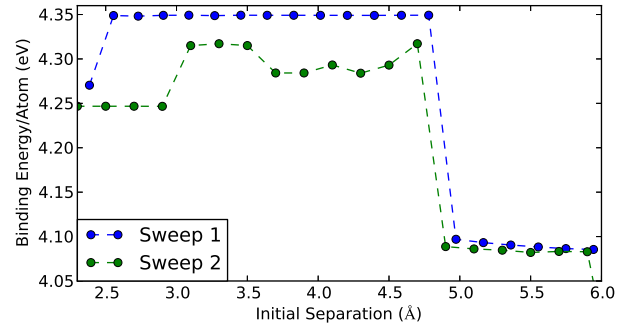


Fig. 7. Geometry sweep for clusters AuGe_{12} : where the CG-relaxed geometry and corresponding E_B (eV) are shown as a function of initial Au-Ge separation. The input structures of Sweep 1 and 2 are described in the text.

turned dense clusters with high binding energies for short Au-Ge distances and dissociated clusters with low binding energies at long Au-Ge distances. This paper focuses on the intermediate clusters which retained two Ge_6 cages connected by Au atoms. Generally within a broad range of d_{init} , these intermediate clusters are nearly identical after CG relaxation. From these intermediate isomers we present those with relatively high binding energies.

Figure 7 shows two geometry sweeps for AuGe_{12} , where each point represents a separate isomer. Each sweep produces compact clusters at $d_{\text{init}} < 2.5\text{\AA}$, intermediate clusters at $2.5 < d_{\text{init}} < 5.0\text{\AA}$, and dissociated clusters at higher separations. Sweep 1, with four Au-Ge interconnects, produces I_1 in the range $2.5 < d_{\text{init}} < 5.0\text{\AA}$, and yields low E_B structure V_1 at $d_{\text{init}} = 2.5\text{\AA}$. Sweep 2, with two Au-Ge interconnects, produces many isomers: II_1 - III_1 observed where $3.0 < d_{\text{init}} < 3.6\text{\AA}$, IV_1 in the range $3.8 < d_{\text{init}} < 4.8\text{\AA}$, and VI_1 and VII_1 at $2.2 < d_{\text{init}} < 3.0\text{\AA}$. We show the geometries of I_1 and II_1 in Fig. 8 and III_1 - VII_1 in Fig. S2. We conclude that the geometry differences within a sweep are small and the overall range of E_B/atom between isomers is less than 0.1 eV, indicating near degeneracy of the clusters. Interesting differences include those of II_1 and III_1 , where III_1 is twisted about its long axis compared with II_1 . V_1 is considerably more octahedral than I_1 .

In each group $\text{Au}_n\text{Ge}_{12}$, $n = 1 - 3$, we identified a few highest binding energy structures for careful study and present geometry and energy data of their CG relaxations in Table 4. We examine clusters which maintain a recognizable pair of Ge_6 cages throughout a CG relaxation. Differences in energies between the highest and lowest in each group was small, typically less than 0.1 eV. There are no significant trends in the deviation from octahedrality σ_{d_G} with binding energy. Ge-Au-Ge angles θ vary from straight to bent (e.g., there is one structure, II_3 , in the $\text{Au}_3\text{Ge}_{12}$ series that has a near tetrahedral angle). Due to the large number of CG-relaxed $\text{Au}_n\text{Ge}_{12}$ structures summarized in this table, we show only four representative structures in Fig. 8, which will be used to contrast properties of stability to those of instability in Sec. 3.5.

Table 4. Calculated average skeletal distances (\AA) and deviations from octahedrality (\AA) of the CG-relaxed clusters $\text{Au}_n\text{Ge}_{12}$ shown in Figs. 8 and S2. Also shown, ranges for bond lengths d_G , d_{AG} , d_A , and values for the angles θ connecting Au to the two cages and energy E_B (eV).

AuGe_{12}	\bar{d}_G	σ_{d_G}	d_{AG}		d_G	θ	E_B
I_1	2.731	0.242	2.66		2.58-3.29	104°	4.349
II_1	2.663	0.127	2.46		2.53-2.86	180°	4.317
III_1	2.664	0.127	2.465		2.51-2.88	180°	4.315
IV_1	2.689	0.189	2.49		2.55-2.94	180°	4.284
V_1	2.703	0.086	2.53		2.54-2.77	114°	4.270
VI_1	2.673	0.124	2.49		2.57-2.83	180°	4.266
VII_1	2.652	0.028	2.46		2.63-2.69	180°	4.247
$\text{Au}_2\text{Ge}_{12}$	\bar{d}_G	σ_{d_G}	d_{AG}	d_A	d_G	θ	E_B
I_2	2.735	0.343	2.46-2.51	2.89	2.50-3.76	171.4° - 176°	4.292
II_2	2.837	0.443	2.42-2.52	2.90	2.48-3.83	117 - 176°	4.291
III_2	2.709	0.232	2.52-2.64	2.81	2.52-3.14	172.5°	4.256
IV_2	2.654	0.063	2.46	4.09	2.57-2.72	148°	4.241
$\text{Au}_3\text{Ge}_{12}$	\bar{d}_G	σ_{d_G}	d_{AG}	d_A	d_G	θ	E_B
I_3	2.653	0.063	2.46-2.50	4.15	2.56-2.71	130 – 138°	4.191
II_3	2.661	0.048	2.49-2.81	3.45-3.59	2.58-2.73	109 – 175°	4.187
III_3	2.685	0.056	2.48-2.52	3.06	2.62-2.76	136 – 151°	4.181
IV_3	2.683	0.142	2.50-2.54	2.97	2.51-2.93	112 – 139°	4.145
V_3	2.760	0.356	2.51-2.69	2.78-2.94	2.52-3.74	174°	4.135

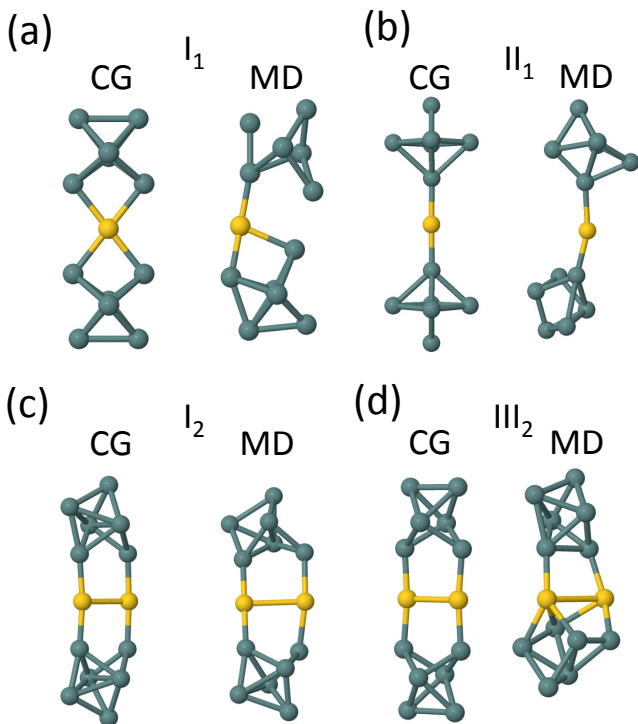


Fig. 8. Examples of $\text{Au}_n\text{Ge}_{12}$ clusters up CG relaxation (left) and post-MD (right). (a) $n = 1$, structure I_1 ; (b) $n = 1$, structure II_1 ; (c) $n = 2$, structure I_2 ; (d) $n = 2$, structure III_2 . Au atoms are gold and Ge are gray.

The remainder of the structures listed in this table can be found in Fig. S2. We show $n = 3$ structures in Sec. 3.6, since we observe no stable neutral $\text{Au}_3\text{Ge}_{12}$ clusters, but see that additional charge supports a prism-like intercluster bridge.

Fig. 8(a) and (b) compares isomers I_1 and II_1 , with four and two Ge-Au-Ge intercluster links. The octahedra of I_1 are more deformed than II_1 , with σ_{d_G} larger by 0.12\AA , the Au-Ge bonds are longer in I_1 by 0.2\AA , and E_B is greater by approximately 0.03 eV. Likewise (c) and (d) compares isomers I_2 and III_2 . Here I_2 is less symmetric than III_2 (C_{2v} vs. D_{2h}) which coincides with reduced octahedrality in I_2 ($\sigma_{d_G} = 0.343\text{\AA}$). II_2 (Fig. S2) is similar to I_2 , with more exaggerated asymmetry ($\sigma_{d_G} = 0.443\text{\AA}$), while IV_2 (Fig. S2) is similar to III_2 with a strongly bent Ge-Au-Ge link (172.5° vs 148°) and a widely separated Au-Au distance (4.09\AA). The overall symmetry change between the isomers of $\text{Au}_2\text{Ge}_{12}$ appears to have direct consequences for the overall cluster stability.

The DOS of the $\text{Au}_n\text{Ge}_{12}$ clusters generally resembles that of $\text{Au}_3\text{Ge}_{18}$ where the Ge $4p$ orbitals dominate just below E_F with some overlap with the Au $5d$ states. The Ge $4p$ and Au $5d$ states of I_1 have less overlap than II_1 . The DOS of I_2 and III_2 are qualitatively similar, but the additional symmetry of III_2 promotes E_F above the energy gap of I_2 , indicating an electronic instability. However, it is not clear from DOS alone which clusters will be stable, but some additional insights are available with COHP analysis (Sec. 3.7). We see the most overlap between Ge and Au orbitals in $\text{Au}_3\text{Ge}_{12}$ due to the greater magnitude of the Au states, but it is clear from MD studies (Sec. 3.5) that this does not contribute to a stability of the $\text{Ge}_6\text{Au}_n\text{Ge}_6$

Table 5. Calculated average skeletal distances and deviations from octahedrality (\AA) of the post-MD clusters Ge_{12} .

	$(\bar{d}_G)_1$	$(\sigma_{d_G})_1$	d_G			
Ge_6	2.72	0.27	2.48-3.36			
Ge_6^{2-}	2.69	0.03	2.63-2.72			
Ge_{12}	$(\bar{d}_G)_1$	$(\sigma_{d_G})_1$	$(\bar{d}_G)_2$	$(\sigma_{d_G})_2$	d_G	
I_0	2.721	0.139	2.757	0.173	2.49-3.00	
II_0	2.710	0.265	2.773	0.360	2.43-3.48	
III_0	2.767	0.292	2.732	0.278	2.51-3.35	

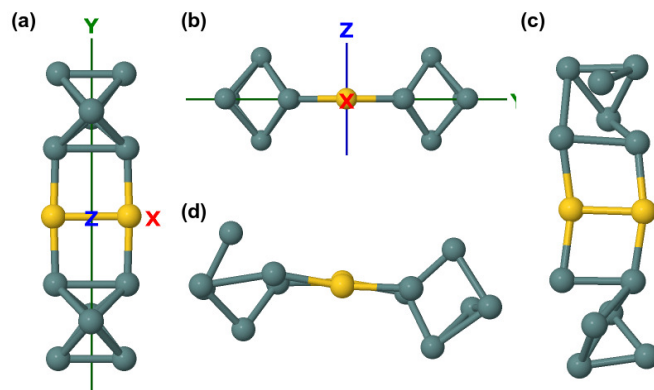
motif when $n = 3$. We present the HOMO and LUMO of selected $\text{Au}_n\text{Ge}_{12}$ clusters in Figs. S3-S7 where delocalized bonding is apparent in the LUMO states of $n = 1, 3$ and the HOMO states in $n = 2$ $\text{Au}_n\text{Ge}_{12}$ clusters.

3.5 Sampling Bond Stability: Molecular Dynamics Studies

Here we test cluster stability using MD simulations to examine structural conformations of clusters at finite temperatures. We run simulations of clusters at 600K for 1000 timesteps of 2 fs each[63], and characterize the post-MD structure in detail after ensuring it is representative of the atomic positions seen throughout the simulation. In applying such methods, the Ge_6 , Ge_9 , and Z_0 clusters retain very similar geometries under MD. We show in Table 5 that the primary differences between CG-relaxed and post-MD structures are small deformations that lead to an overall symmetry loss. Since Ge-Ge bonds elongate considerably in the cage environment supported with delocalized bonding, we do not attempt to distinguish bonds based on their distances [58].

In Ge_{12} and $\text{Au}_n\text{Ge}_{12}$ stability is determined primarily on the formation/breaking of intercluster bonds and the preservation of octahedrality of the Ge_6 cages which may deform beyond recognition during the MD simulation. I_0 retains two intercluster bonds and measurably octahedral Ge_6 cages as shown in Fig. 3(b). II_0 breaks its intercluster bond but its Ge_6 clusters remain cage-shaped. With structure III_0 , an intercluster bond breaks, and the relative tilting of the two cages has changed. In all cases, the deviation from octahedrality σ_{d_G} is larger in the post-MD structures, the overall symmetry of the cluster is reduced, and the average skeletal Ge-Ge bond length has increased (as quantified in Table 5).

In Fig. 5 we compare the post-MD structures of $\text{Au}_3\text{Ge}_{18}$ and $\text{Au}_3\text{Ge}_{18}^{5-}$ to the previously described CG structures. The neutral cluster forms two additional Au-Ge bonds, and the right hand Ge_9 cage opens forming a larger cage including the three Au atoms. The $\text{Au}_3\text{Ge}_{18}^{5-}$ maintains the motif of two Ge_9 cages separated to an Au triangle since it does not form new Au-Ge bonds. In both clusters the Ge-Ge cage bonds elongate and one Au-Au bond becomes widely separated. The COHP (Sec. 3.7) and will confirm the tendency of the Au-Au bonds to separate.

**Fig. 9.** The $\text{Au}_2\text{Ge}_{12}^{4-}$ cluster with (a-b) CG relaxation and (c-d) post-MD.

Next we compare the post-MD structures of $\text{Au}_n\text{Ge}_{12}$ to the previously described CG structures and describe the geometry differences in Table 6. In Fig. 8 we see I_1 (a) breaks an Au-Ge intercluster bond, while II_1 (b) maintains both: merely twisting about its Ge-Au-Ge intercluster link so $\theta_{\text{Ge-Au-Ge}}$ remains close to linear. When comparing the two predominant isomers of AuGe_{12} , the four Au-Ge intercluster bonds of I_1 are less stable than the two of II_1 . We observe in $n = 2$ that stability under MD simulation appears to rely on more than number of intercluster links: the asymmetric I_2 and II_2 structures are stable under MD while the relatively symmetric III_2 and IV_2 structures are not although each have four linear Au-Ge intercluster links. This is consistent with the asymmetric coupling of the Ge_9 clusters in $[\text{Au}_3\text{Ge}_{18}]^{5-}$. We see that $\text{Au}_3\text{Ge}_{12}$ does not readily form linear stable Ge-Au-Ge links, whether the relative Ge_6 orientations are symmetric or asymmetric. However in the following section we discuss the additional stability of the $\text{Au}_3\text{Ge}_{12}$ cluster with an ionic charge.

3.6 Stability of Charged Clusters

The influence of charge on cluster shape, dictated largely by Wade's rules, is an essential consideration in Ge cluster studies. We briefly describe the effect of a charge $q = 2$ and $q = 4$ on some isomers of $\text{Au}_n\text{Ge}_{12}^{q-}$, with a focus on how the presence of additional charge stabilizes linear Ge-Au-Ge intercluster links in $\text{Au}_2\text{Ge}_{12}$ and $\text{Au}_3\text{Ge}_{12}$. To obtain these results, we ran identical geometry sweeps to our neutral charge calculations (Sec. 3.4), with charge $q = 2$ and $q = 4$ added to the cluster. Rather than present every new isomer observed, we show the CG-relaxed and post-MD geometries of $\text{Au}_2\text{Ge}_{12}^{4-}$ in Fig. 9 and that of $\text{Au}_3\text{Ge}_{12}^{2-}$ in Fig. 10, where the additional charge has stabilized structures not observed in neutral clusters. Properties of these isomers, including the combined octahedrality of the Ge_6 clusters, are summarized in Table 7.

Table 7 lists two stable isomers that were found for $\text{Au}_2\text{Ge}_{12}^{2-}$. The primary difference is in the linearity of

Table 6. Results for the calculated average skeletal distances and deviations from octahedrality (\AA) of the $\text{Au}_n\text{Ge}_{12}$ clusters after MD runs, where a blank in a σ_{d_G} column indicates a complete disordering of the octahedra. Also shown, values for the angles θ connecting Au to the two cages and energy, E_B (eV). Structures are shown in Figs. 8 and S2.

AuGe_{12}		d_{AG}	θ	$(\bar{d}_G)_1$	$(\sigma_{d_G})_1$	$(\bar{d}_G)_2$	$(\sigma_{d_G})_2$	d_G	
I ₁		2.46, 2.76	166°	2.74	0.32	2.79	0.40	2.36-3.51	
II ₁		2.45, 2.60	163°	2.74	0.40	2.73	0.23	2.42-3.95	
$\text{Au}_2\text{Ge}_{12}$		d_A	d_{AG}	θ	$(\bar{d}_G)_1$	$(\sigma_{d_G})_1$	$(\bar{d}_G)_2$	$(\sigma_{d_G})_2$	d_G
I ₂	3.20	2.49-2.66	163°, 177°	2.779	0.379	2.743	0.309	2.53-3.73	
II ₂	3.03	2.47-2.73	173°	2.774	0.318	2.812	0.409	2.43-3.87	
III ₂	3.42	2.41-2.84	102°-157°	2.696	0.298	—	—	2.39-3.56	
IV ₂	3.27	2.38-2.73	125°-163°	2.726	0.251	—	—	2.49-3.41	
$\text{Au}_3\text{Ge}_{12}$		d_A	d_{AG}	θ	$(\bar{d}_G)_1$	$(\sigma_{d_G})_1$	$(\bar{d}_G)_2$	$(\sigma_{d_G})_2$	d_G
I ₃	3.04	2.46-3.04	75° – 169°	—	—	—	—	—	2.52-3.21
II ₃	3.60-3.71	2.48-3.01	100° – 175°	2.68	0.11	—	—	—	2.54-2.99
III ₃	3.25-3.68	2.43-2.91	96° – 165°	2.81	0.28	—	—	—	2.54-3.53
IV ₃	2.75	2.45-2.89	127° – 143°	2.73	0.19	—	—	—	2.37-3.29
V ₃	2.77	2.48-2.84	150°	2.81	0.37	—	—	—	2.51-3.83

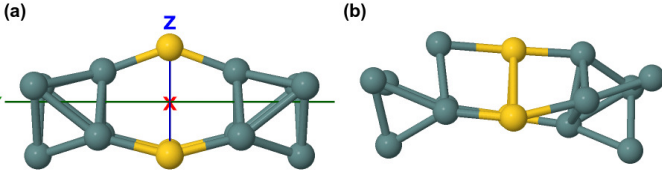


Fig. 10. The $\text{Au}_3\text{Ge}_{12}^{2-}$ cluster with (a) CG relaxation and (b) post-MD. The three Au atoms form a triangle in the x-z plane, and the lower, back Au atom is hidden from view.

the Ge-Au-Ge links and the degree of octahedrality, with lower energy isomer having $\theta = 148.5^\circ$, like the neutral IV₂, and $\sigma_{d_G} = 0.05\text{\AA}$. Nearly degenerate is the isomer with $\theta = 178.5^\circ$, like the neutral III₂. When the charge is increased to $q = 4$, only the linear-link isomer is observed, which is also stable under MD simulation. Likewise we observed a stable isomer of $\text{Au}_3\text{Ge}_{12}^{q-}$ with both $q = 2$ and $q = 4$. While the CG-relaxed $\text{Au}_3\text{Ge}_{12}^{2-}$ still has bent Ge-Au-Ge links ($\theta = 140^\circ - 149^\circ$), the post-MD structure has one nearly linear bond ($\theta = 178^\circ$), and the bridging structure resembles a prism. This structure type was simply not observed in the neutral cluster.

In contrast to the neutrally charged isomers, we observe linear links in both $\text{Au}_2\text{Ge}_{12}^{q-}$, $q = 2$ and $q = 4$ with D_{2h} symmetry (as III₂) that are stable under MD simulation. Moreover we observe stable $\text{Au}_3\text{Ge}_{12}^{q-}$ clusters. While a more complete exploration of both value of q and possible linking structures could be performed, this work confirms that additional charge stabilizes linear Ge-Au-Ge cluster interconnections.

3.7 COHP Analysis of Bonding

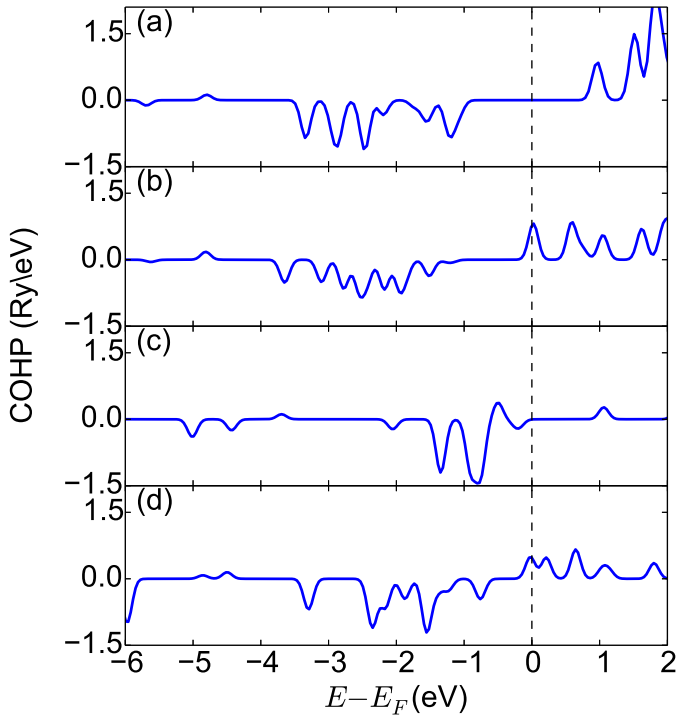
By examining post-MD structures, we observe features of stable $\text{Au}_n\text{Ge}_{12}$ clusters which are not apparent merely from CG simulation. Given the computational expense of MD, it is desirable to have other methods to determine bond stability. Here we employ COHP electronic partitioning, as described in Sec. 2, to characterize stability in terms of electronic structure.

Figure 11 shows the COHP of the Ge-Ge bonds of the four CG-relaxed Ge_{12} structures. The groundstate Z_0 , Fig. 11(a), introduces the typical criterion of a stable cluster: the states switch from negative bonding to positive antibonding MOs at the Fermi level. In structure I₀, Fig. 11(b), the anti-bonding states first appears at E_F at the top of the band gap. Given the overall stability of this cluster, this suggests the additional states introduced in the DOS (see Sec. 3.1) from the intercluster Ge_6 - Ge_6 interaction are antibonding, and serve to keep the cluster as two separate, linked structures. Structure II₀, Fig. 11(c), has antibonding states below E_F at the base of the energy gap, which can be correlated with the dissociation into two Ge_6 clusters in the post-MD structure. Cluster III₀, Fig. 11(d), appears metallic with the first antibonding state at E_F (much like I₀) and a small energy gap. This is consistent with the post-MD rearrangements: the CG-relaxed structure of III₀ has three intercluster bonds and forms two during the MD run. We tentatively conclude that two intercluster Ge-Ge bonds provide a relatively stable connecting structure between Ge_6 octahedral cages.

We use the structures shown in Fig. 8 to compare the properties of stable CG-relaxed $\text{Au}_n\text{Ge}_{12}$ clusters: II₁ is compared to the less stable I₁ in AuGe_{12} and I₂ to less stable III₂ $\text{Au}_2\text{Ge}_{12}$. We show their COHP interactions in three figures: Ge-Ge in Fig. 12; Au-Ge in Fig. 13; and Au-

Table 7. Calculated properties of the CG-relaxed clusters found in geometry sweeps for charged clusters $\text{Au}_n\text{Ge}_{12}^{q-}$. Also shown, the properties for these clusters post-MD.

CG Properties						
	\bar{d}_G	σ_{d_G}	d_{AG}	d_A	d_G	θ
$\text{Au}_2\text{Ge}_{12}^{2-}$ (1)	2.66	0.05	2.49	3.92	2.56-2.73	148.5°
$\text{Au}_2\text{Ge}_{12}^{2-}$ (2)	2.70	0.15	2.53	2.84	2.53-2.95	178.5°
$\text{Au}_2\text{Ge}_{12}^{4-}$	2.72	0.09	2.59	2.89	2.51-2.84	176°
$\text{Au}_3\text{Ge}_{12}^{2-}$	2.67	0.06	2.58-2.75	3.14-4.0	2.51-2.84	140° – 149°
$\text{Au}_3\text{Ge}_{12}^{4-}$	2.73	0.13	2.76	3.23-3.72	2.59-2.93	155°
MD Properties						
	\bar{d}_G	σ_{d_G}	d_{AG}	d_A	d_G	θ
$\text{Au}_2\text{Ge}_{12}^{2-}$ (1)	2.67	0.11	2.46-2.48	3.80	2.35-4.05	140°, 157°
$\text{Au}_2\text{Ge}_{12}^{2-}$ (2)	2.72	0.23	2.38-2.60	3.82	2.40-2.88	149°, 157°
$\text{Au}_2\text{Ge}_{12}^{4-}$	2.79	0.17	2.62-2.70	2.76	2.51-3.26	161° – 164°
$\text{Au}_3\text{Ge}_{12}^{2-}$	2.75	0.15	2.37-2.73	3.22-3.96	2.43-2.99	146° – 178°
$\text{Au}_3\text{Ge}_{12}^{4-}$	2.82	0.24	2.58	2.93-4.16	2.58-3.39	135° – 171°

**Fig. 11.** COHP analysis of Ge-Ge interactions Ge_{12} after CG relaxation. Structures (a) Z_0 , (b) I_0 , (c) II_0 , and (d) III_0 .

Au in Fig. 14. Generally we see that the primary indicator of stability is that of the Au-Ge interaction.

In AuGe_{12} the overall similarities of the Ge-Ge interaction of are apparent in Fig. 12 (a-b) where a single, large bonding peak appears below E_F at $E - E_F \approx -2.0$ eV. However I_1 shifts from Ge-Ge bonding to antibonding states at E_F while II_1 has a small antibonding state in Ge-Ge at E_F . In the Au-Ge interaction [Fig. 13 (a-b)], I_1 has antibonding states at E_F , while II_1 has no Au-Ge state at E_F . Instead E_F is centered between occupied bonding

and empty antibonding states. Given the lower stability of I_1 , this indicates the Ge-Ge antibonding state arises from intercluster interaction, like that of I_0 , but does not break the structure. The antibonding Au-Ge state at E_F of I_1 is likely to cause the Au-Ge bond breaking observed in the post-MD cluster, whereas those in II_1 merely twist.

The Ge-Ge COHP curves of $\text{Au}_2\text{Ge}_{12}$ I_2 and III_2 are qualitatively similar [Figs. 12(c,d)]. Neither cluster has antibonding states below E_F , and the primary difference is the shift in the location of E_F from I_2 to III_2 . Significantly, while the Au-Ge interactions of I_2 have no antibonding character below E_F [Fig. 13(c)], there is an antibonding interaction in III_2 [Fig. 13(d)], again confirming that antibonding states in Au-Ge below E_F are correlated with cluster instability. In examining COHP curves of $\text{Au}_3\text{Ge}_{12}$, there are as many as three antibonding states below E_F in Au-Ge interactions, thus it is unsurprising that no neutral stable clusters were observed.

We see no overall stability trends in the Au-Au COHP results. In Fig. 14 we show the Au-Au COHP results of (a) I_2 and (b) III_2 . In both cases, there are significant anti-bonding MO's below E_F . For comparison, we examine $\text{Au}_3\text{Ge}_{18}$, and present its COHP analysis in Fig. 15. We note three features in this figure: in (a) the Au-Au interaction has strong antibonding states at E_F , in (b) Au-Ge has a weak antibonding state at E_F (this disappears in the post-MD structure), and in (c) Ge-Ge is bonding up to E_F , whereas below E_F indicating no intercluster antibonding states between Ge_9 clusters. In terms of antibonding states, the Au-Au COHP is consistent with that observed for $\text{Au}_2\text{Ge}_{12}$. This character remains in the COHP analysis of the the charged $\text{Au}_3\text{Ge}_{18}^{5-}$. To further examine this antibonding state the electronic structure analysis should account for aurophilic Au-Au interactions as discussed in Refs. [17,35].

Generally the COHP of the charged systems are qualitatively similar to their neutral counterparts with E_F moved beyond E_{gap} into the antibonding states. It is clear

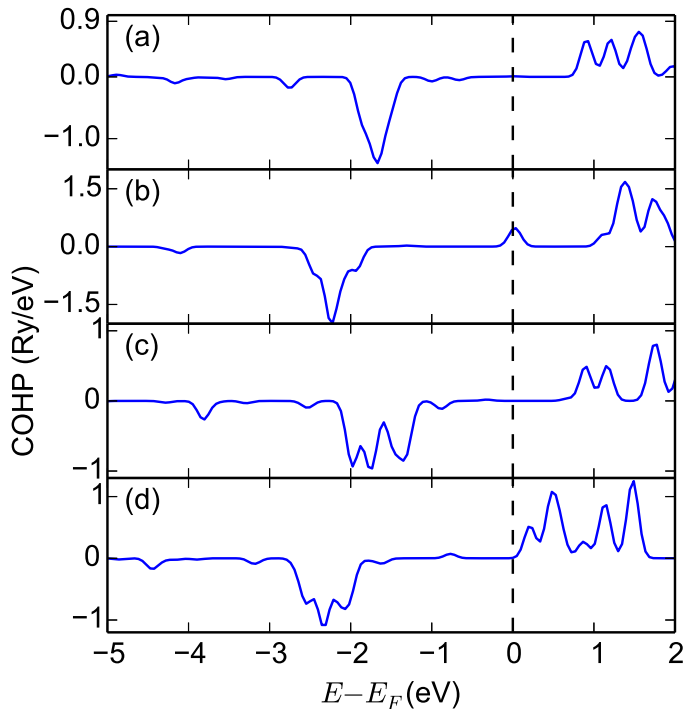


Fig. 12. COHP for Ge-Ge bonds for $\text{Au}_n\text{Ge}_{12}$ where (a) I_1 , (b) II_1 , (c) I_2 , (d) III_2

this is not a good predictor of the stability of charged states. This reflects the DFT treatment of charge rather than nature herself.

3.8 Extended $\infty_2[\text{Au}_2\text{Ge}_6]$ Structures

To extend our exploration of the ability of Ge_6 cages to bond with Au atoms, we consider crystalline Au-Ge structures built with this geometry. The precedent studies include Ref. [62], where 1D, 2D, and 3D structures formed of Ge_9 cages are examined. We show the hypothetical structure $\infty_2[\text{Au}_2\text{Ge}_6]$ in the inset of Fig. 16 which represents the isomer observed with binding energy maximum at $d_{\text{init}} = 2.6\text{\AA}$. Here, Au atoms are placed in the positions of the radial non-bonding orbitals of isolated $[\text{Ge}_6]^{2-}$ clusters in the xy plane. Following the techniques of Sec. 3.4, we vary the initial Au-Ge distance, perform CG minimization, and find the binding energy and relaxed geometry (Fig. 16). The relaxed structure features a subunit of a Ge_6 octahedron with four radial Au-Ge bonds. Each subunit is spaced closely to form a 2D crystal structure including Au-Au bonds. The binding energy has a peak at $d_{\text{init}} = 2.6\text{\AA}$, where d_{init} is the initial Au-Ge bondlength. The average bond found in the Ge cages is $\bar{d}_G = 2.72 \pm 0.06\text{\AA}$, showing that the bonds are elongated compared to the isolated clusters, but the cages are close to octahedral. Ge-Ge bonds range from $d_G = 2.62 - 2.77\text{\AA}$, which includes those in the two-dimensional plane forming a square with lengths of approximately 2.65\AA and the out-of-plane bonds are 2.77\AA . The Au-Ge bond lengths $d_A = 2.42\text{\AA}$ are short compared with the clusters studied in Sec. 3.2 and

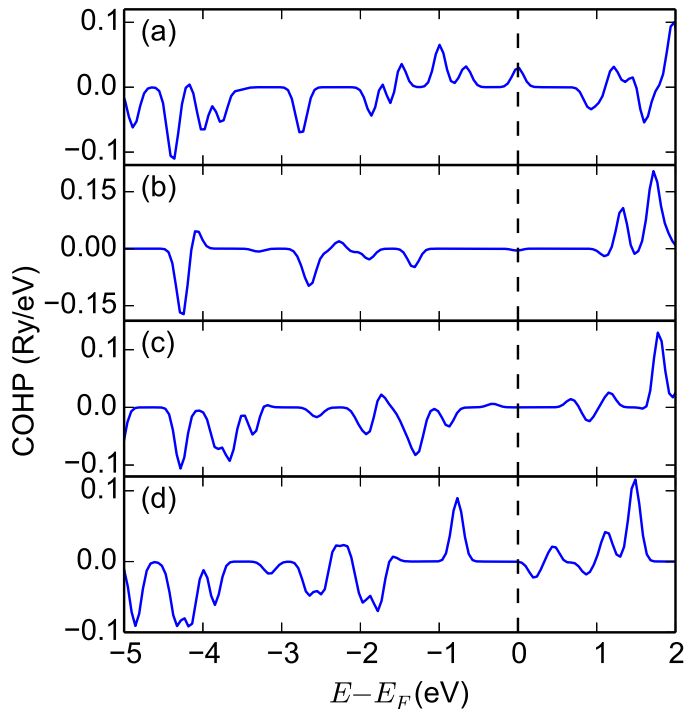


Fig. 13. COHP for Au-Ge bonds for $\text{Au}_n\text{Ge}_{12}$ where (a) I_1 , (b) II_1 , (c) I_2 , (d) III_2 .

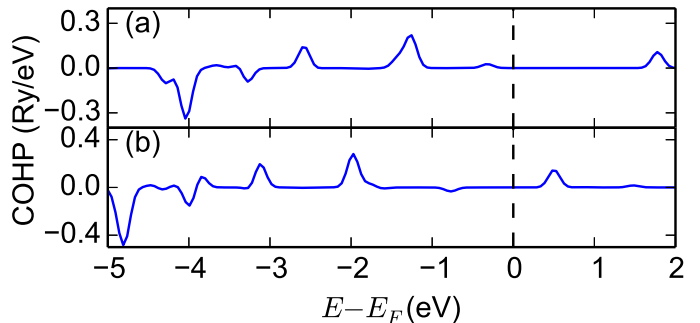


Fig. 14. COHP for Au-Au bonds for $\text{Au}_2\text{Ge}_{12}$, where (a) I_2 , (b) III_2 .

the Au-Au bond is $d_A = 2.85\text{\AA}$. The Ge-Au-Ge linking angle is 117° . We explored other stoichiometries, such as $\infty_1[\text{Au}_1\text{Ge}_6]$, $\infty_1[\text{Au}_2\text{Ge}_6]$, and $\infty_2[\text{Au}_4\text{Ge}_6]$, and observed considerably less smooth E_B vs. d_{init} curves, indicating these stoichiometries prefer dissociation or non-octahedral geometries in the input structures we examined. Again we see that a Au-Ge ratio of 1:6 seems to support greater overall stability in Au-Ge systems.

4 Discussion and Conclusions

Beyond its well known properties as a covalently bonded sp^3 semiconductor, the versatility in the Ge electronic structure allows it to form cage-like structures with extended bond lengths. Taken in isolation, cages Ge_6 and Ge_9 need additional electrons to stabilize their delta-hedral shapes; two electrons being sufficient for the former,

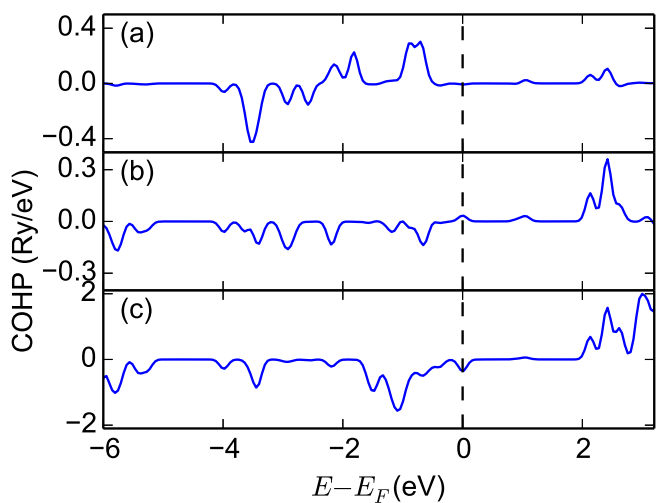


Fig. 15. COHP for $\text{Au}_3\text{Ge}_{18}$ where for interactions (a) Au-Au, (b) Au-Ge, and (c) Ge-Ge.

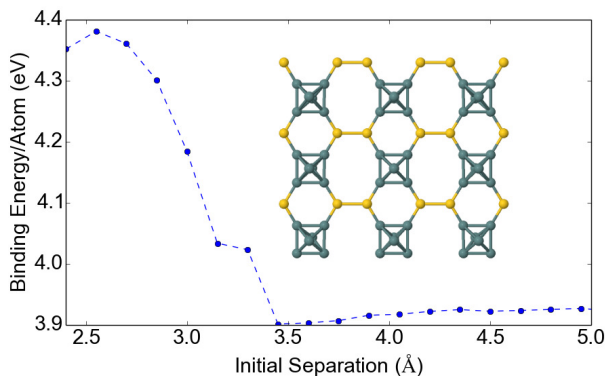


Fig. 16. Binding energy E_B (eV) versus d_{init} (Å) of extended structure $[\text{Au}_2\text{Ge}_6]_{\infty}$. The inset shows the geometry of this local E_B maxima found with CG minimization for $d_{\text{init}} = 2.6\text{Å}$.

and four for the latter, consistent with Wade’s Rules. By using DFT methods, we have examined the stability of combinations of octahedral Ge_6 cages in various forms. In examining linking structures between two such cages, we found that two bonds form and stabilize Ge_{12} , especially when the two clusters are aligned symmetrically with Ge-Ge bonds connecting the two equatorial planes of the octahedra. Other orientations are less stable, as can be seen using COHP analysis or by running brief MD simulations to examine how the cluster evolves. There are hints in these runs that 5-atom and 7-atom rings can form, similar to those found in clathrate and allo-Ge [24, 25].

By combining Au with Ge, new possibilities emerge. It is tantalizing that through linking to a triangle of Au atoms, deltahedral Ge_9 cages stabilize in the charged $[\text{Au}_3\text{Ge}_{18}]^{5-}$. In analogy, this paper addressed whether Ge_6 cages could be linked into $\text{Au}_n\text{Ge}_{12}$ clusters for $n = 1 - 3$. We observe stable isomers of readily form in AuGe_{12} and $\text{Au}_2\text{Ge}_{12}$, but not $\text{Au}_3\text{Ge}_{12}$. This appears largely due

to the nature of the overlap in molecular orbitals at the highest occupied level: it is relatively simple to favor the radially directed Au-Ge bonds in $n = 1 - 2$ systems, and difficult in $n = 3$. We also observe additional stability provided by asymmetric combinations of $n = 2$ systems and charge in both $n = 2 - 3$ systems. Our conclusion is that stable Au-Ge clusters or perhaps even extended structures are most likely to be found if 1-2 Au atoms are used to interconnect the equatorial planes of the octahedra, assuming external ligands or large spacing ions were employed to counterbalance ionicity. This suggests that geometry and charge state play a larger role in stable intercluster links than chemical species consistent with Wade’s rules.

We emphasize the importance of DFT to treat metal-semiconductor bonds in cage-like clusters, especially with the relativistic nature of valence electrons in Au. We recognize that the details of our results will be sensitive to the details of the DFT calculation. More over, there are fundamental problems with DFT methods, e.g., dispersion forces and their effects on MD results. In any DFT study, the selection of basis orbitals and the type of exchange-correlation functional may significantly alter some predictions. We have found SIESTA to have several positive virtues for this study, including its ability to partition electronic states and to study isolated multiply charged clusters.

As in many cluster studies, it is easy to get lost in the task of finding groundstate structures. We have been systematic in our choices of structures to study, and have found by CG minimization the usual large number of structures and their binding energies. While a more comprehensive sampling procedure would surely yield more information about definitive ground-state structures in vacuum, especially in $\text{Au}_3\text{Ge}_{12}$, this method revealed geometries that could be supported with external ligands. Importantly the observation of the same, or very similar, isomers over a range of initial Au-Ge separations is an assurance of cluster stability to small vibrations and perturbations.

A very helpful tool has been the use of COHP electronic partitioning to examine the stability of these clusters. Since COHP is calculated from orbital interactions that neglect exchange and correlation, it is an imperfect measure of bonding in DFT systems, yet we observe trends which suggest such analysis may be used to understand overall Au-Ge cluster stability. To test the COHP analysis, we have also used brief MD simulations to see whether a given structure is stable enough not to “shake apart” or have significant rearrangement of atoms during a run. Our work shows that strongly antibonding Au-Ge orbitals at E_F will tear apart intercluster bonds. We expect experimental realizations of these systems to feature stronger Au-Au bonds as in Ref. [17] which notes the concept of aurophilicity, much like hydrogen bonds, that is not readily treated in DFT methods.

A question of this study was whether Au atoms would maintain much of their metallic bonding character in the compounds. And if Au connects two Ge cages, we observe that the bonding is more covalent, Au tending to be the

single interconnect between two Ge atoms. We have observed different behavior in more dense clusters, such as one Au bonding to multiple Ge atoms in a cluster, but our primary interest was in a direct analogy to the experimentally observed [Au₃Ge₁₈]⁵⁻.

Remaining still as a theoretical challenge are such problems as is the kinetic nature of Au's role in crystallizing Ge [3] or forming diamond-structure nanowires [11]. Recent work [64] in nanowire growth observes metastable crystalline AuGe catalysts which may further inform which geometries are favored in these nano-sized clusters. Our brief MD studies were not sufficient to make progress in this challenge. But perhaps understanding better Au-Ge bonds in existing compounds should be the center of future studies of this fascinating pair of elements.

Acknowledgements

This research was supported in part by the assistance and resources of the Notre Dame Center for Research Computing, particularly Paul Brenner and Timothy Stitt.

References

- H. Okamoto and T. B. Massalski, *Bull. Alloy Phase Diagrams* **5** (1984) 601
- R. M. Waghorne, V. G. Rivlin, and G. I. Williams, *J. Phys. F: Met. Phys.* **6** (1976) 147
- Z. Tan, S. M. Heald, M. Rapposch, C. E. Bouldin, and J. C. Woicik, *Phys. Rev. B* **46** (1992) 9505
- R. Pöttgen, H. Borrmann, C. Felser, O. Jepsen, R. Henn, R. K. Kremer, and A. Simon, *J. Alloys Comp.* **235** (1996) 170
- Q. Lin and J. D. Corbett, *J. Am. Chem. Soc.* **134** (2012) 4877
- C. Blumenstein, J. Schäfer, S. Mietke, S. Meyer, A. Dollinger, M. Lochner, X. Y. Cui, L. Patthey, R. Matzdorf, and R. Claessen, *Nat. Phys.* **7** (2011) 776
- J. Wu and J. L. Coffey, *Adv. Mater.* **20** (2008) 1571
- S. Kodambaka, J. Tersoff, M. C. Reuter, and F. M. Ross, *Science* **316** (2007) 729
- E. Sutter and P. Sutter, *Nano Lett.* **8** (2008) 411
- S. A. Dayeh and S. T. Picraux, *Nano Lett.* **10** (2010) 4032
- D. Wang and H. Dai, *Angew. Chemie* **114** (2002) 4977
- A. D. Gamalski, C. Ducati, and S. Hofmann, *J. Phys. Chem. C* **115** (2011) 4413
- S. Ryu, C. R. Weinberger, M. I. Baskes, and W. Cai, *Model. Simul. Mater. Sci. Eng.* **17** (2009) 075008
- A. M. Dongare, M. Neurock, and L. V. Zhigilei, *Phys. Rev. B* **80** (2009) 184106
- C. Schenk and A. Schnepf, *Angew. Chemie Int. Ed.* **46** (2007) 5314
- A. Spiekermann, S. D. Hoffmann, F. Kraus, T. F. Fässler, *Angew. Chem. Int. Ed.* **46** (2007) 1638
- A. Spiekermann, S. D. Hoffmann, T. F. Fässler, I. Krossing, and U. Preiss, *Angew. Chem. Int. Ed.* **46** (2007) 5310
- S. C. Sevov, *Intermetallic Compounds: Vol. 3, Principles and Practice*, J. H. Westbrook and R. L. Fleischer (John Wiley & Sons, Ltd, Chichester, UK, 2002) 113
- K. Wade, *J. Chem. Soc. D Chem. Commun.* **20** (1971) 792
- A. J. Welch, *Chem. Commun.* **49** (2013) 3615
- E. Zintl, *Angew. Chemie* **52** (1939) 1
- G. S. Armatas and M. G. Kanatzidis, *Nature* **441** (2006) 1122
- D. Sun, A. E. Riley, A. J. Cadby, E. K. Richman, S. D. Krolann, and S. H. Tolbert, *Nature* **441** (2006) 1126
- F. Kiefer, A. J. Karttunen, M. Döblinger, and T. F. Fässler, *Chem. Mater.* **23** (2011) 4578
- A. M. Guloy, R. Ramlau, Z. Tang, W. Schnelle, M. Baitinger, and Y. Grin, *Nature* **443** (2006) 320.
- T. F. Fässler, H.-J. Muhr, and M. Hunziker, *Eur. J. Inorg. Chem.* **1998** (1998) 1433
- P. Kircher, G. Huttner, K. Heinze, and G. Renner, *Angew. Chemie Int. Ed.* **37** (1998) 1664
- G. Renner, P. Kircher, G. Huttner, P. Rutsch, and K. Heinze, *Eur. J. Inorg. Chem.* **2000** (2000) 879
- A. F. Richards, H. Hope, and P. P. Power, *Angew. Chemie* **42** (2003) 4071
- S. Ögüt and J. R. Chelikowsky, *Phys. Rev. B* **55** (1997) R4914
- R. B. King, I. Silaghi-Dumitrescu, and A. Kun, *J. Chem. Soc. Dalton Trans.* **2002** (2002) 3999
- L.-Z. Zhao, W.-C. Lu, W. Qin, Q.-J. Zang, C. Z. Wang, and K. M. Ho, *Chem. Phys. Lett.* **455** (2008) 225
- D. Sánchez-Portal, P. Ordejón, E. Artacho, J. M. Soler, *Int. J. Quantum Chem.* **65** (1997) 453
- J. M. Soler, E. Artacho, J. D. Gale, A. García, J. Junquera, P. Ordejón, and D. Sánchez-Portal, *J. Phys. Condens. Matter*, **14** (2002) 2745
- H. Schmidbaur and A. Schier, *Chem. Soc. Rev.* **37** (2008) 1931
- S.-D. Li, Z.-G. Zhao, H.-S. Wu, and Z.-H. Jin, *J. Chem. Phys.* **115** (2001) 9255
- W. Xu, Y. Zhao, Q. Li, Qianshu, Y. Xie, Yaoming, and H. F. Schaefer III, *Mol. Phys.* **102** (2004) 579
- S. Yoo and X. C. Zeng, *J. Chem. Phys.* **124** (2006) 184309
- W. Qin, W.-C. Lu, L.-Z. Zhao, Q.-J. Zang, G.-J. Chen, C. Z. Wang, and K. M. Ho, *J. Chem. Phys.* **131** (2009) 124507
- X.-J. Li and K.-H. Su, *Theor. Chem. Acc.* **124** (2009) 345
- X. Li, K. Su, X. Yang, L. Song, and L. Yang, *Comput. Theor. Chem.* **1010** (2013) 32
- J. E. Kingcade Jr., U. V. Choudary, and K. A. Gingerich, *Inorg. Chem.* **18** (1979) 3094
- N. Korber, *Angew. Chem. Int. Ed.* **48** (2009) 3216
- B. T. Truong and M. T. Nguyen, *J. Phys. Chem. A* **115** (2011) 9993
- D. Selli, I. A. Baburin, R. Martoňák, and S. Leoni, *Sci. Rep.* **3** (2013) 1466
- R. Dronskowski and P. E. Blöchl, *J. Phys. Chem.* **97** (1993) 8617
- N. Troullier and J. Martins, *Phys. Rev. B* **43** (1991) 1993
- L. Kleinman and D.M. Bylander, *Phys. Rev. Lett.* **48** (1982) 1425
- W. Kohn and L. J. Sham, *Phys. Rev.* **140** (1965) A1133
- O. F. Sankey and D. J. Niklewski, *Phys. Rev. B* **40** (1989) 3979
- J. P. Perdew, K. Burke, and M. Ernzerhof, *Phys. Rev. Lett.* **77** (1996) 3865
- E. Anglada, J. M. Soler, J. Junquera, and E. Artacho, *Phys. Rev. B* **66** (2002) 205101

53. <http://departments.icmab.es/leem/siesta/Documentation/Manuals/manuals.html>
54. E. Fernández, J. Soler, I. Garzón, and L. Balbás, *Phys. Rev. B* **70** (2004) 165403
55. E. Fernández, J. Soler, and L. Balbás, *Phys. Rev. B* **73** (2006) 235433
56. M. Torres, E. Fernández, and L. Balbás, *Phys. Rev. B* **71** (2005) 155412
57. S. Nosé, *J. Chem. Phys.* **81** (1984) 511
58. When we examine a structures geometry visually, we use the Jmol software package with its software bond defaults, which is the combined covalent radii plus 0.45Å. Thus when drawn in Jmol, the maximal Ge-Ge, Au-Ge, and Au-Au bonds are at distances of 2.80, 3.12, and 3.45Å, respectively.
59. R. B. King, I. Silaghi-Dumitrescu, and M. M. Uță, *J. Chem. Soc. Dalton Trans.* **2007** (2007) 364
60. S. Bulusu, S. Yoo, and X. C. Zeng, *J. Chem. Phys.* **122** (2005) 164305
61. R. B. King, and I. Silaghi-Dumitrescu, *Inorg. Chem.* **42** (2003) 6701
62. A. J. Karttunen, T. F. Fässler, M. Linnolahti, and T. A. Pakkanen *ChemPhysChem* **11** (2010) 1944
63. Due to the computational expense of MD simulation, we limit the duration of our runs to 2 fs. While CG runs for clusters typically take on the order of 5 hrs on 8 cores, the MD simulations of the same cluster, as described in the methods section, take roughly 36 hrs on 8 cores with 2.4 GHz processors and 12 GB RAM. http://wiki.crc.nd.edu/wiki/index.php/Available_Hardware
64. A. D. Gamalski, J. Tersoff, R. Sharma, C. Ducati, and S. Hofmann, *Phys. Rev. Lett.* **108** (2012) 255702

5 Supplementary Material

In Fig. S1 we show the Highest Occupied Molecular Orbital (HOMO) and Lowest Unoccupied Molecular Orbital (LUMO) for the CG-relaxed cluster $\text{Au}_3\text{Ge}_{18}$. These figures clearly show the asymmetry of the two Ge_9 cages. In the LUMO pictures, the right cage shows extended π -like hybridization connecting into triangle of Au atoms. The nodal structure of the orbitals for both cages changes from HOMO to LUMO. Note, COHP for the Au-Au bonds of this cluster is shown in Fig. 15.

In Tables 4 and 6, a number of clusters $\text{Au}_n\text{Ge}_{12}$, $n = 1, 2, 3$, are listed and described. Four figures were picked as being representative examples for the main paper and are shown in Fig. 8 (specifically, I_1 , II_1 , I_2 , and III_2). The remainder of those clusters are shown in Fig. S2. Clusters III_1 through VII_1 are shown only after CG minimization since the isomers have the same overall symmetry and number of bonds as I_1 and II_1 , and thus exhibit similar behavior under MD simulation. The rest are shown after both CG minimization and MD simulation.

We show HOMO and LUMO states for five selected CG-relaxed clusters of $\text{Au}_n\text{Ge}_{12}$. COHP analysis is also shown for four of these five clusters in Sec. 3.7. In Fig. S3, we show two orientations each for AuGe_{12} , cluster I_1 . Referring back to Fig. 8(a), we see that it is highly symmetric. An interesting feature is the spherical orbital centered on the Au atom, seen in (a) and (c), connecting only loosely to the extended π -like orbitals of the two cages. In the LUMO, (b) and (d), the center Au atom is not directly connected to the cages. As discussed in Sec. 3.7, this cluster is less stable than cluster II_1 , we show the post-MD rearrangement and symmetry breaking of I_1 in Fig. 8(a).

In Fig. S4, we show the orbitals after CG minimization for the more stable $n = 1$ cluster II_1 . Cluster II_1 is again highly symmetric [Fig. 8(b)] but interestingly, the HOMO state is degenerate and shows very localized electronic density on the cages, with very minimal interaction with the central Au atom in this orbital. The LUMO state, Fig. S4(c), has electronic structure for the Au bridge site that is similar to that shown in Fig. S3(b), that is, an extended π -like orbital that does not include the central Au atom. The orientations of the cages relative to the bridging Au are different for I_1 and II_1 , as seen when comparing Figs. S3 to S4 or comparing the CG picture for I_1 of Fig. 8(a) to the one for II_1 in Fig. 8(b).

As Figs. S3 and S4 corresponded to Figs. 8(a) and (b), in Figs. S5 and S6, we show the HOMO and LUMO states for $n = 2$, which correspond to the images of CG-relaxed structures in Figs. 8(c) and (d). As discussed in Sec. 3.7, cluster I_2 , Figs. S5 and 8(c), is more stable than cluster III_2 , Figs. S6 and 8(d). The cage orbitals for the HOMO state for $n = 2$ are less extended than for $n = 1$. Because of the relative tilting of the two cages for I_2 , the two Au atoms participate differently in the bonding in the HOMO, Fig. S5. In contrast, for III_2 shown in Fig. S6, both Au atoms are equally involved in bonding to each other in the HOMO, and not at all in the LUMO.

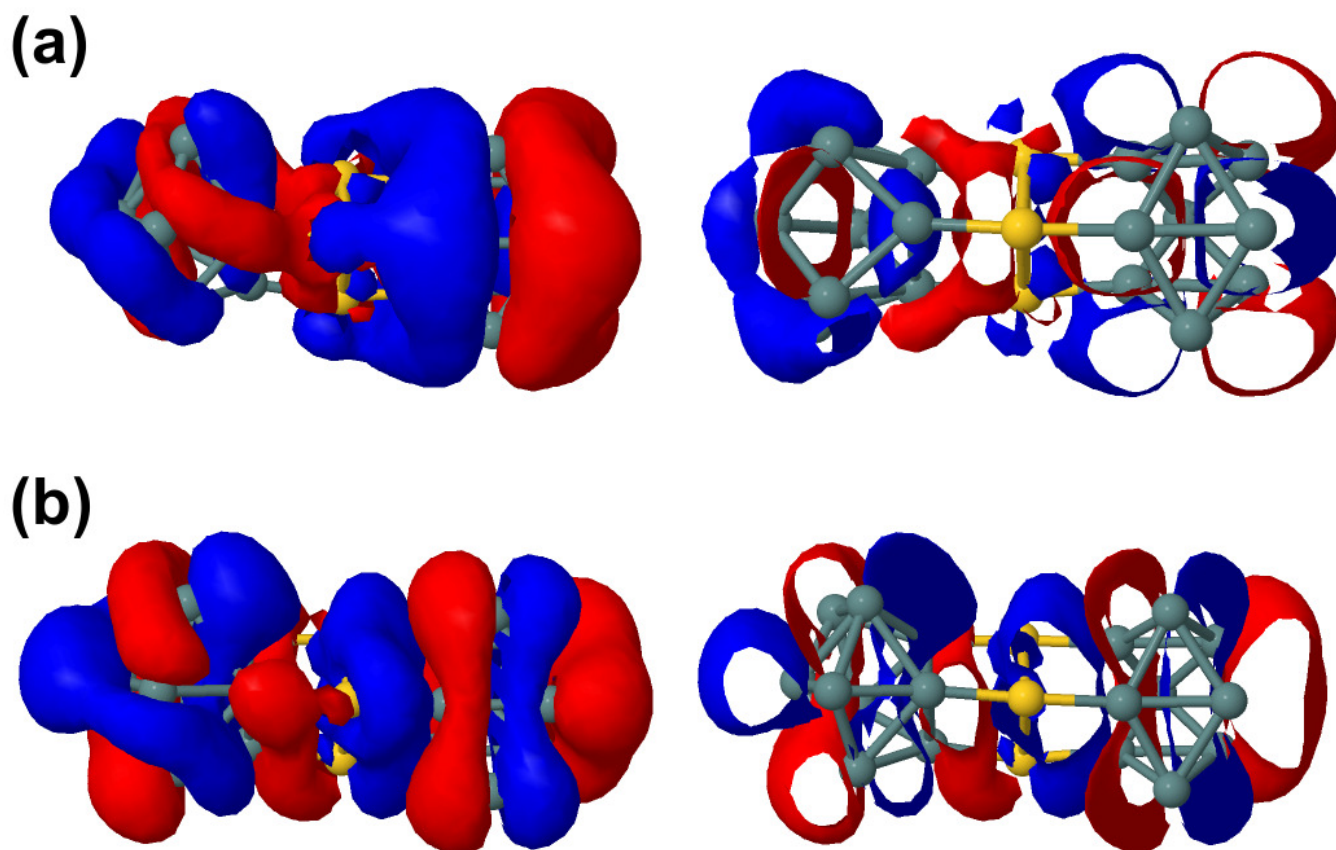


Fig. S1. (a) HOMO and (b) LUMO of neutral $[\text{Au}_3\text{Ge}_{18}]$ where the right column is a slice of the 3D orbitals shown on the left.

As seen in Fig. S2, all $n = 3$ clusters change significantly after a MD run. In Fig. S7, we show HOMO and LUMO for cluster I_3 to compare these with its CG-relaxed geometry [Fig. S2(h)]. The tilting of the two cages causes two of the three Au atoms to participate differently in the bonding in the HOMO and in the LUMO states. It is most interesting to compare this with the HOMO and LUMO states for $\text{Au}_3\text{Ge}_{18}$, Fig. S1. Here we see that the cage electrons in $\text{Au}_3\text{Ge}_{12}$ are much more localized than in $\text{Au}_3\text{Ge}_{18}$.

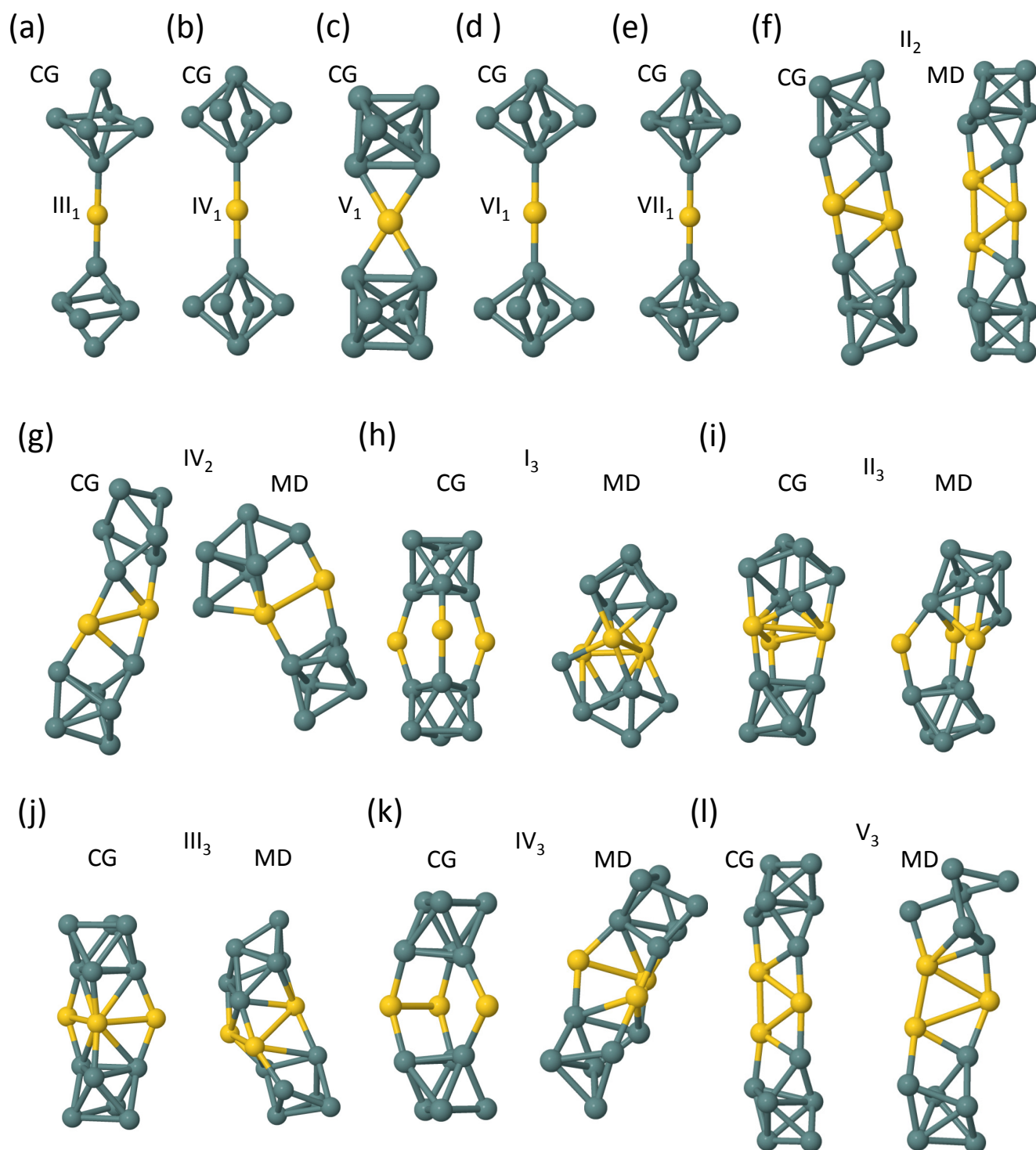


Fig. S2. Clusters of Au_nGe_{12} : (a)-(e), $n = 1$, III_1 , IV_1 , V_1 , VI_1 , VII_1 ; (f) and (g), $n = 2$, II_2 and (b) IV_2 ; (h) - (l); $n = 3$, I_3 , II_3 , III_3 , IV_3 , V_3 . For $n = 1$, clusters are shown only for after CG minimization. Cluster IV_1 only differs from VI_1 due to a smaller horizontal cross section. For $n = 2, 3$, clusters are shown after CG minimization and also after a MD run.

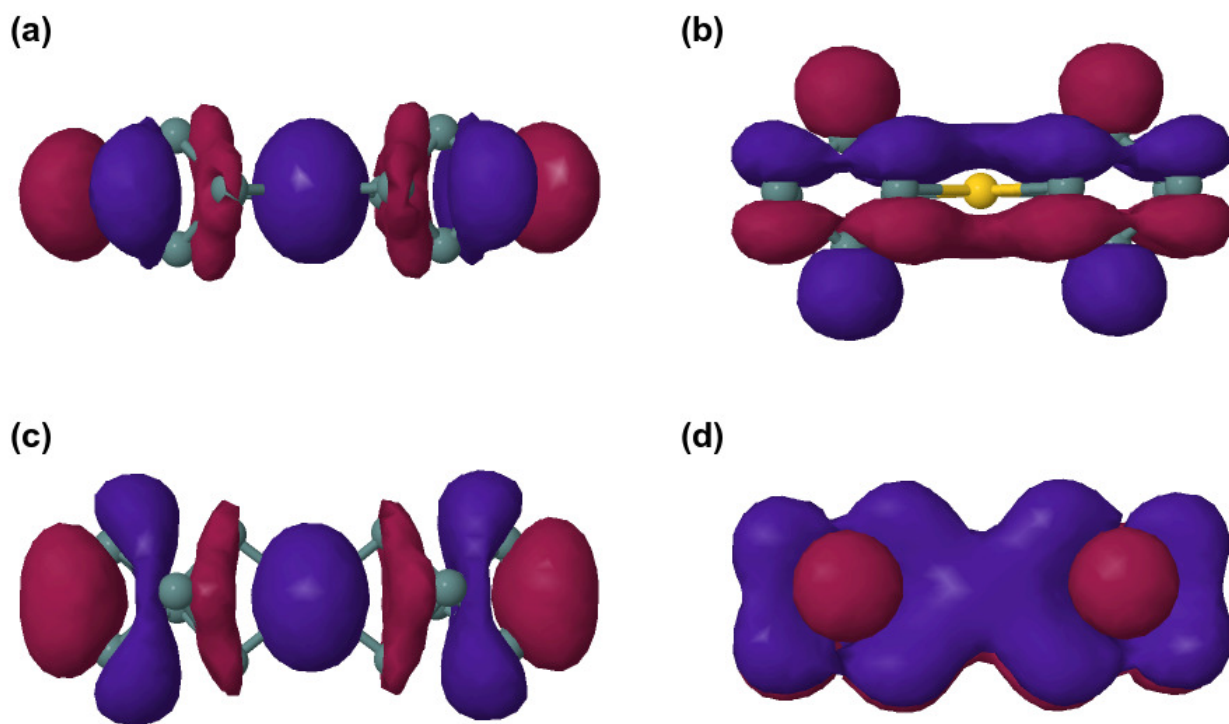


Fig. S3. (a,c) HOMO and (b,d) LUMO of neutral AuGe_{12} I_1 .

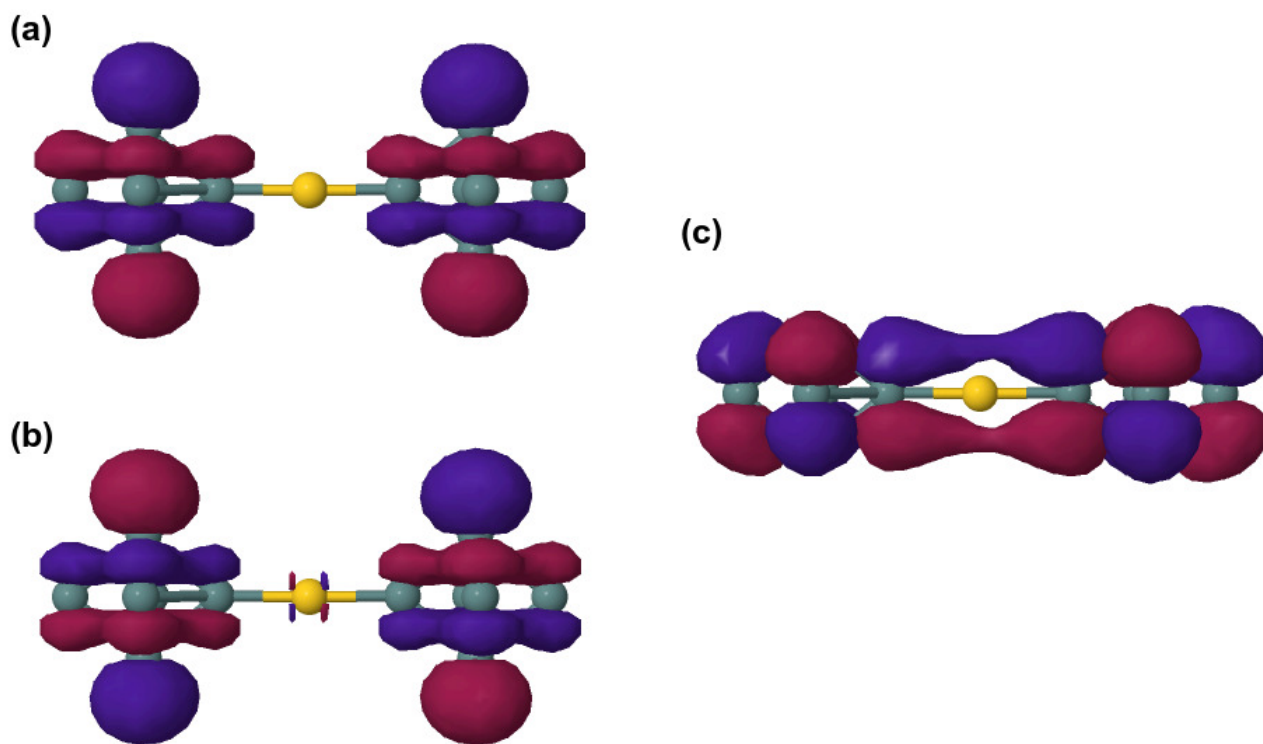


Fig. S4. (a,b) Degenerate HOMO and (c) LUMO of neutral AuGe_{12} II_1 .

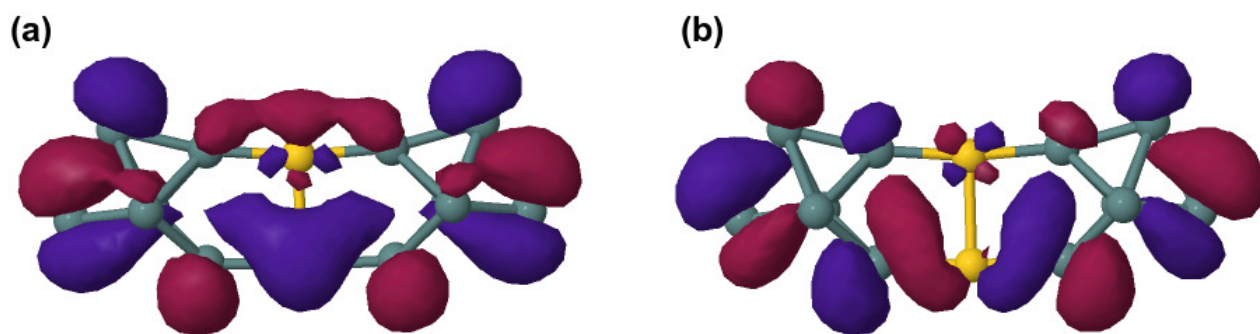


Fig. S5. (a) HOMO states and (b) LUMO of neutral $Au_2Ge_{12} I_2$.

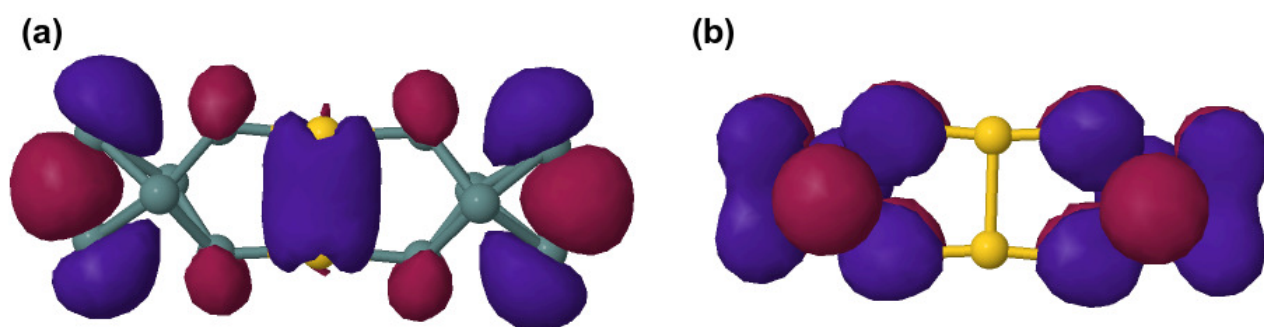


Fig. S6. (a) HOMO and (b) LUMO of neutral $Au_2Ge_{12} III_2$.

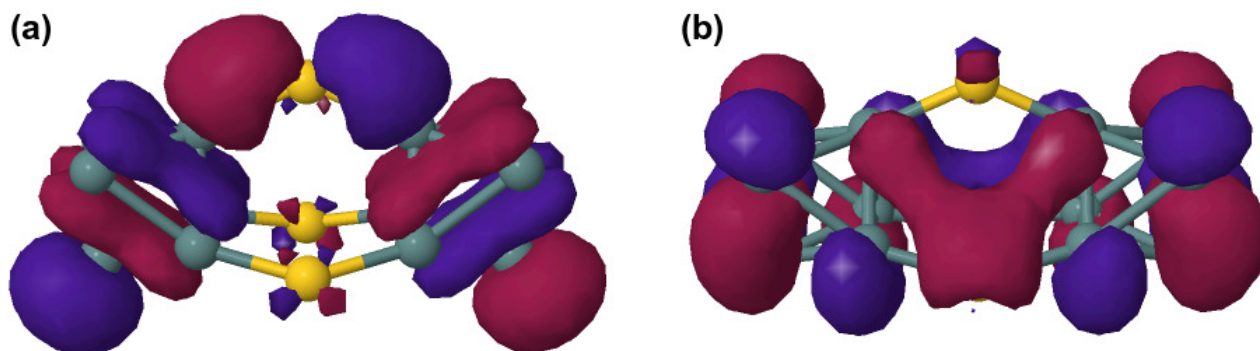


Fig. S7. (a) HOMO and (b) LUMO of neutral $Au_3Ge_{12} I_3$.